DEPENDENCE OF CROSS SECTIONS FOR MULTI-ELECTRON LOSS BY 6 MeV/amu Xe^{18+} IONS ON TARGET ATOMIC NUMBER

A Thesis

by

YONG PENG

Submitted to the Office of Graduate Studies of
Texas A&M University
in partial fulfillment of the requirements for the degree of

MASTER OF SCIENCE

May 2003

Major Subject: Chemistry

DEPENDENCE OF CROSS SECTIONS FOR MULTI-ELECTRON LOSS BY 6 MeV/amu Xe^{18+} IONS ON TARGET ATOMIC NUMBER

A Thesis

by

YONG PENG

Submitted to Texas A&M University
in partial fulfillment of the requirements
for the degree of

MASTER OF SCIENCE

Approved as to style and content by:

Rand L. Watson
(Chair of Committee)

John Reading
(Member)

Sherry J. Yennello
(Member)

Emile A. Schweikert
(Head of Department)

May 2003

Major Subject: Chemistry

ABSTRACT

Dependence of Cross Sections for Multi-electron Loss by 6 MeV/amu Xe^{18+} Ions on Target Atomic Number. (May 2003)

Yong Peng, B.A., Sichuan University

Chair of Advisory Committee: Dr. Rand L. Watson

It has been proposed to use heavy ion beams with energies around 10 MeV/amu, masses around 200, and average charges of 1+ as a driver for inertial fusion reactor. Current designs require the beams to travel through a region where the background gas pressure is several milli-torr. Thus, it is important to assess the rate at which the charge state of an incident beam evolves while passing through the background gas. The first objective of this project is to study the dependence of cross sections for multi-electron loss on target atomic number by using 6 MeV/amu Xe^{18+} ions and to compare the results with the n-body Classical Trajectory Monte Carlo calculations. A secondary objective of this project is to determine the extent to which the cross sections for molecular targets can be represented as sum of the cross sections for their atomic constituents.

Cross sections for loss of one through eight electrons from 6 MeV/amu Xe^{18+} in single collisions have been measured with noble gas targets. The target Z-dependence of the total loss cross section was found to be well represented by two straight line segments. The cross section for He and Ne define one straight line segment and those for Ar, Kr and Xe define the other, where the second line exhibits a smaller slope. The

predictions of n-CTMC calculations are in good agreement with the measured total electron loss cross sections. A semiempirical fitting procedure based on the independent electron approximation provided a reasonably good representation of the individual cross sections for all of the noble gas targets. Additional measurements performed with a variety of molecular targets provided a rigorous test of cross section additivity and showed that the additivity rule works well for electron loss from heavy ions in the present energy and charge regime. A semiempirical calculation based the IEA shows that the average most probable impact parameter for electron loss is much smaller than the target molecular bond length. This result is believed to account for the finding of the insensitivity of the electron loss cross section to molecular structure.

To my parents and my family

ACKNOWLEDGMENTS

It is a pleasure to thank my patient and encouraging coworkers and friends at the Cyclotron Institute.

It is difficult to overstate my gratitude to Dr. Rand L. Watson, my advisor, for his constant support, encouragement and guidance throughout this research project. His own enthusiastic and conscientious attitude towards work, methodical approach to a problem, cautious experimentation and attention to details, and critical technical writing have made me realize the significance of these traits in any type of endeavor. His patience and understanding during this project were also deeply appreciated. His enthusiasm, his inspiration, and his great efforts to explain things clearly and simply, helped to make this project fun for me. I would have been lost without him.

I appreciate Dr. Sherry J. Yennello, Dr. John Reading and Dr. John Hardy for serving on my committee and helping with my thesis and defense.

I am also grateful to my research colleague, Dr. Vladimir Horvat, for his invaluable assistance with the experiments, discussions, and data analysis. Whenever I faced problems, his help was always there.

Special thanks must be given to Dr. Perumal Appathurai for his help during my thesis writing, especially his patience for the thesis corrections.

I also appreciate Miss Anna Allred and Mr. August L. Keksis for their help in my thesis writing. Officemates, Lijun Qing, Wei Liu and Xiaodong Tang deserve my thanks for their stimulating discussions.

My greatest gratitude goes to the entire Cyclotron staff and personnel for their assistance all the time. The support from the Welch Foundation is greatly acknowledged.

My special thanks to my wife, Hongyu Liu, and my children, Jenny and Emily, whose love and support has been an inspiration in all aspects of my life.

Finally, and most importantly, my very special thanks to my wonderful parents to whom I owe everything. Without their constant encouragement and love, this would have never become a reality. I dedicate this thesis to them.

TABLE OF CONTENTS

Page

ABSTRACT iii

ACKNOWLEDGMENTS vi

TABLE OF CONTENTS viii

LIST OF FIGURES x

LIST OF TABLES xiii

CHAPTER

I INTRODUCTION 1

II EXPERIMENTAL SETUP 7

A. Beam line 7
B. Gaseous targets 11
C. Detector system 16
1. Position Sensitive Microchannel Plate Detector (PSD) 16
2. Data acquisition 18

III DATA ANALYSIS METHODS 21

A. Charge distribution and growth curves 21
B. Cross section determination 26

IV RESULTS AND DISCUSSION 29

A. Target Z-dependence of electron loss by 6 MeV/amu Xe^{18+} 29
1 Cross sections for collisions with noble gas targets 30
2. Dependence of electron loss cross sections on Δq 33

CHAPTER Page

3. Z-dependence of the total loss cross sections 33
4. Single electron capture 39
5. Semi-empirical method for systematizing the $\sigma(\Delta q)$ 41
B. Molecular targets and cross section additivity 48
1. Cross sections for molecular gases 48
2 The dependence of total loss cross sections on target average atomic number 52
3. Additivity rule 54
4. The effect of molecular structure on the electron loss cross sections 56
5. Average electron loss per collision 67

V CONCLUSIONS 69

REFERENCES 72

VITA 76

LIST OF FIGURES

FIGURE Page

1. Schematic diagram of an inertial confinement fusion (ICF) target 2

2. Schematic diagram of experimental setup. 8

3. Schematic diagram of differentially pumped gas cell..... 10

4. Target gas manifold system.. 12

5. Illustration of the structure of a Microchannel plate (MCP)..... 17

6. An enlarged view of one channel of the MCP and the principle of its gain. 17

7. Schematic diagram of electronics for data analysis. The position was determined by comparing the top signal to the sum of the top and bottom signals. 20

8. Typical position spectrum of the outgoing projectile charge distribution. The probability of electron loss (q>18+) is much larger than that of electron capture (q<18+). The percentage of charge changed beam is less than 25% of the incident beam. 23

9. Charge fractions for 6 MeV/amu Xe^{18+} plotted as a function of Ne target thickness. Solid lines and filled circles are for electron loss. Dashed line and open circles are for electron capture. The lines show the results of least squares fits of equation 3-2 to the data In the low pressure region, the charge fractions vary linearly with target thickness, but at the higher values of π , substantial deviations from linearity are observed. 25

10. Comparison of the cross sections obtained for 6 MeV/amu Xe^{18+} ions in Ne using the two fitting procedures: with residual gas contribution subtracted (open circles) and without residual gas contribution subtracted..... 27

FIGURE Page

11. Single and multiple electron loss cross sections plotted as a function of the number of electrons removed from the incident 6 MeV/amu Xe^{18+} ions. 32

12. The cross section ratios $(\sigma_1 + \sigma_2)/\sigma_T$ (solid circles) and $(\sigma_T - \sigma_1 - \sigma_2)/\sigma_T$ (solid squares) plotted as a function of the target atomic number. 35

13. Total electron loss cross sections for 6 MeV/amu Xe^{18+} ions colliding with noble gas targets plotted as functions of target atomic number. The dashed line was drawn through the experimental data of helium and neon while the solid line was fit to the experimental data of Ar, Kr and Xe. 36

14. Effective charge ($Z_{2(eff)}$) of the noble gas targets as a function of atomic number. 38

15. Cross sections for single-electron capture by 6 MeV/amu Xe^{18+} from noble gas targets as a function of atomic number. 40

16. Schematic diagram showing the differential area associated with collisions having impact parameters between b and b+db. 42

17. Electron loss cross sections plotted as a function of the number of electrons removed from the incident Xe^{18+} projectile (filled symbols). The solid lines and empty symbols show the results of fits to the data using the semiempirical IEA prescription described in the text. 45

18. The fitting parameters p_0 and δ in the semiempirical IEA prescription described in the text plotted as functions of the target atomic number. 47

19. Total loss cross section (per atom) for 6 MeV/amu Xe^{18+} projectile in various molecular targets plotted as a function of target average atomic number. The dashed line is the same line that was defined by the He and Ne data points (shown here by empty circles) in figure 13. 53

FIGURE Page

20. Ratio of the measured total electron loss cross section and the cross section calculated using the additivity rule expressed by equation (4-11), plotted versus the target average atomic number. 55

21. Comparison of cross sections for the loss of one to eight electrons in the molecular targets N_2, CO, and CO_2. Average atomic numbers are indicated in parentheses 57

22. Comparison of cross sections for the loss of one to eight electrons in the molecular targets O_2, C_3F_8, and CF_4. Average atomic numbers are indicated in parentheses 58

23. Comparison of cross sections for the loss of one to eight electrons in the molecular target SF6, and atomic target Ne. Average atomic numbers are indicated in parentheses..... 59

24. Calculated $\sigma_n^{'}$ vs. impact parameter b for one to eight electron loss in collision with sulfur atoms 62

25. The most probable impact parameters for one to eight electron loss are plotted as a function of the target atomic number. 64

26. The most probable impact parameter plotted as a function of Δq. 65

27. Schematic diagram comparing the most probable impact parameters for one-electron loss collisions of 6 MeV/amu Xe^{18+} with S and F atoms to the S-F bond length in SF_6. The radii are defined in the text. All the units are in Angstroms. 66

28. The average number of electrons lost from 6 Mev/amu Xe^{18+} ions in single collisions as a function of target (average) atomic number. The open circles represent the noble gas targets while solid circles represent the molecular targets. The solid line is fit to the noble gas data..... 68

LIST OF TABLES

TABLE Page

I. The pressure (mTorr) range, and the atomic number or average atomic number of the target gases 11

II. Experimental electron capture and loss cross sections for 6 MeV/amu Xe^{18+} colliding with noble gas targets. Except for helium, individual cross sections were measured for the loss of as many as eight electrons. Those cross sections for which the projectile lost more than 8 electrons were combined together and are listed under the heading >8. 31

III. Calculated cross sections obtained using a semiempirical procedure based on the IEA. The Gaussian distribution $p = p_0 e^{-\frac{b^2}{2\delta^2}}$ was used to represent the single electron loss probability. 46

IV. Comparison of the experimental electron loss cross sections with the cross sections obtained using the semiempirical fitting procedure in absolute percentage; $100\,|\frac{\sigma_{meas} - \sigma_{cal}}{\Delta\sigma_{meas}}|$. The last row lists the calculated $Z_{2(eff)}$ for the noble gases. 46

V. Electron capture and loss cross sections for 6 MeV/amu Xe^{18+} in molecular targets as a function of Δq, the change in projectile charge. All cross sections are in units of Mb/atom. The predicted loss cross sections are calculated by using equation 4-1 49

VI. Radii of the target atoms, and calculated p_0 and δ parameters 61

VII. The most probable impact parameters for electron loss from 6 MeV/amu Xe^{18+} ion in collisions with atomic targets (in Å) 63

VIII. Molecular bond lengths 63

CHAPTER I

INTRODUCTION

High-energy particle collisions with atomic and molecular targets provide fundamental information concerning atomic and molecular structure, and have significant applications in many areas. For example, they play a role in the design of heavy ion accelerators [1], in the development of design criteria for inertial fusion reactors, in the assessment of vacuum requirements for new heavy ion accelerators, in astrophysical phenomena [2], in x-ray astronomy [3], and in the diagnostics and plasma physics of fusion reactors. [4-6].

Scientists have worked for many decades on the problem of developing a controllable fusion reactor to harness fusion energy. One approach is magnetic confinement fusion (MCF) which utilizes magnetic fields to confine low density high temperature plasmas [7]. Another approach, inertial confinement fusion (ICF) reactor, is a kind of thermonuclear internal combustion engine. ICF is essentially a scaled down thermonuclear explosion of sufficiently small size that it can be readily utilized for power production. Inertial confinement means that the inertia of the mass of exploding fuel provides a sufficient confinement time that the thermonuclear reaction can take place before the mass blows apart. A small amount of fusion fuel is compressed to a high density and temperature so it will ignite rapidly and burn efficiently [8]. A schematic diagram of an ICF target is shown in figure 1 [7]. Generally, the capsule is a spherical shell filled with low-density gas (≤ 1.0 mg/cm^3). The ablator is in the outer region and the fuel, frozen or liquid deuterium-tritium

---

This thesis follows the style and format of the journal Physical Review A.

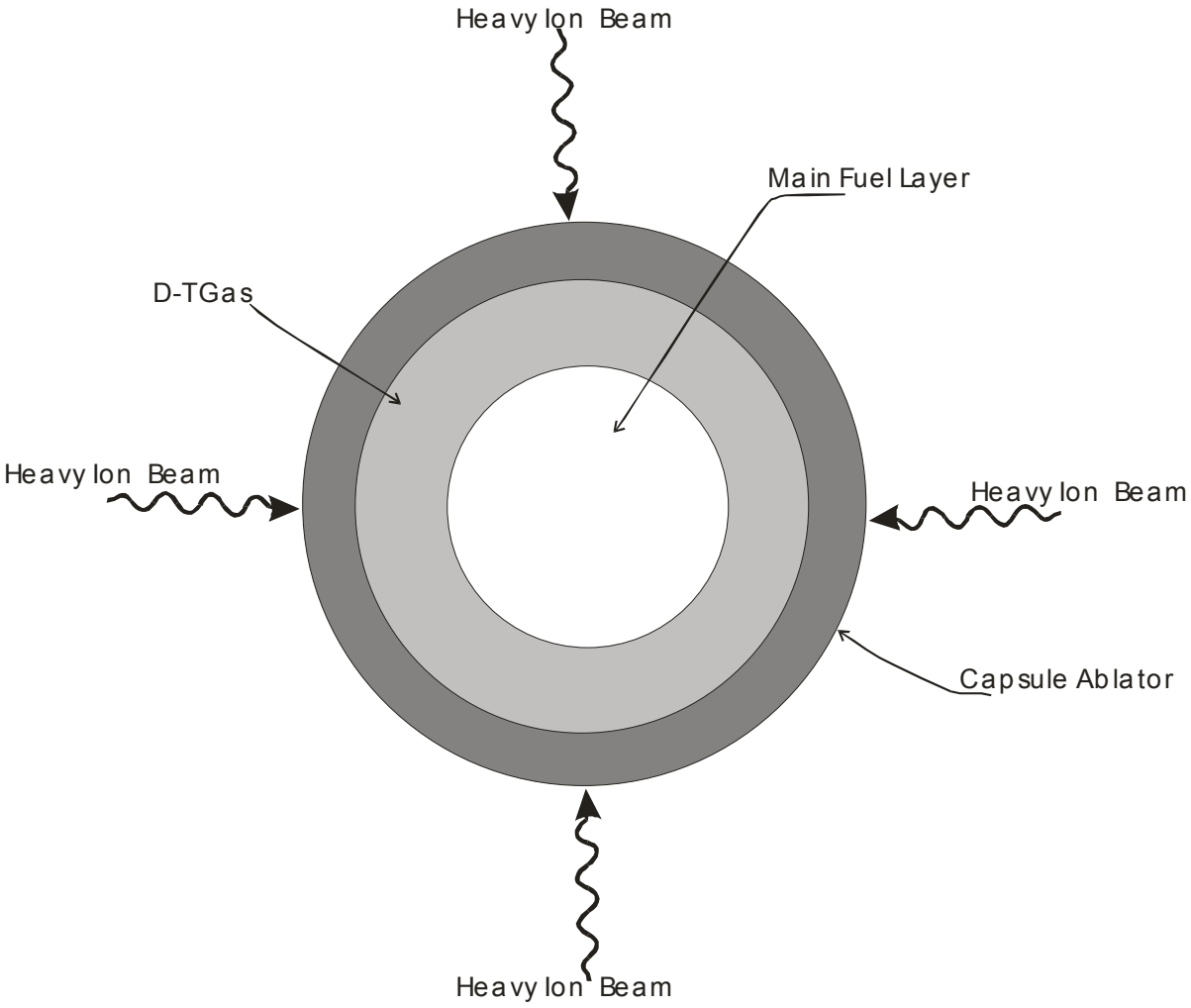

Figure 1. Schematic diagram of an inertial confinement fusion (ICF) target [7]

(DT), is in the inner region. DT is used [9] because its fusion reaction rate is approximately two orders of magnitude larger than that of the next fastest reaction $He(D,P)^4He$ in the relevant temperature range.

Laser or heavy ion beams can be used to transfer energy to the ICF capsules to ignite an implosion. Heavy-ion drivers are superior to lasers in efficiency, durability and repetition rate [9-10], therefore heavy-ion driven fusion reactors have the greatest potential for future inertial fusion power plants.

A method has been proposed to use 10 MeV/amu heavy ions, mass around 200, and average charge state of 1+ as a driver for heavy-ion-driven fusion reactors [10]. Gains are critically dependent on the spot size attainable when the ion beam is focused on the target radiator. Charge changing collisions and scattering by the background vapor limit the quality of the beam focus and hence, it is important to assess the rate at which the charge state of an incident beam evolves while passing through a background gas. Currently, no beam of 10 MeV/amu ions having mass around 200 and charge of 1+ is available. It has been argued, however, that a beam of somewhat lower energy and higher initial charge could be used to test theories that might be capable of providing cross sections for the ion beam of interest [11].

Since the pioneering work of Thompson and Rutherford, theoretical and experimental investigations of energetic particle collisions with matter have continued to provide important information concerning electron transfer and ionization processes. Comprehensive review articles containing valuable information on experimental and theoretical equilibrium and nonequilibrium charge-changing processes have been published by *Nikolaev* [12], *Betz* [13] and *Tawara and Russek* [14]. *Nikolaev*[13] primarily reviewed experimental and theoretical results concerning charge changing cross sections, equilibrium charge state fractions, and average equilibrium charges of fast light ions. *Betz=s* [13] paper

contains theoretical and experimental results for total cross sections and charge state distributions. In addition, this article reviews the results of a number of experiments that have been performed to measure differential charge changing cross sections and to obtain information on the impact-parameter dependence of electron capture and loss by energetic ions. Of particular relevance to the present work is a discussion by Betz concerning the question of cross section additivity for molecular targets. In the review article by *Tawara and Russek* [14], the charge changing processes of hydrogen ions in gases, metal vapors and gaseous carbon are discussed from the experimental point of view. Other relevant review papers include *Allison* [15], *Tawara et al* [16], *Betz* [17] and *Greenland* [18].

In general, the final charge of a projectile depends on the following parameters: projectile atomic number (Z_1), velocity (v_1), incident charge (q), target atomic number (Z_2) and target thickness (π). Determination of the dependence of the charge changing cross sections on each of these parameters requires great amounts of experimental data as well as theoretical treatments. While a considerable amount of work has been performed for low atomic number projectiles, very few experimental investigations have focused on single collisions of high atomic number projectiles in gaseous targets. *Alton et al* [19] measured single- and multiple-electron-loss cross sections with 20-MeV Fe^{4+}on thin targets of the noble gases, H_2, N_2, O_2, CH_4, CO_2, CHF_3 and SF_6. A modification of a formula originally presented by Bohr was modified and shown to give good agreement with the experimental single electron loss cross sections for the noble gas targets. In the case of molecular targets, it was found that the effective atomic number, which was defined as the screened nuclear charge, was not consistent with the average atomic number. When q was greater than 8, the

effective atomic number was greater average target atomic number, otherwise it was less than the average atomic number. In other words, the additivity rule was not satisfied in this collision region.

*Boman et a*l [20] measured the cross sections for 1 MeV/amu oxygen ions in 5+, 6+, 7+ and 8+ charge states passing through gaseous targets of D_2, He, Ne, Ar, and Kr. They found that the single electron loss cross sections depended on Z_2^n where Z_2 is the target atomic number and n ranged from 0.33 to 0.98 for change state 7+ down to 5+, respectively, for the noble gas targets. The cross sections for the molecular target D_2, however, did not follow this empirical law. *Olson* [21] used the n-body classical trajectory Monte Carlo method to estimate the cross-sections for electron loss from fast, low charge state ions (20 MeV/amu Xe^{q+} and 40MeV/amu Bi^{q+}, q=1-12) in collisions with BeF_2. His calculations indicated that multiple electron loss represented a serious problem for schemes that propose to employ low charge state heavy ions for inertial fusion. In the recent work of *Mueller et al.* [22], using 3.4 MeV/amu Kr^{7+} and Xe^{11+} ions, it was reported that the average number of projectile electrons removed in a single collision with a nitrogen atom was 1.86 for Kr and 1.97 for Xe.

In the present investigation, a 6 MeV/amu Xe^{18+} ion beam was used to examine the dependence of the cross sections for multi-electron loss on target atomic number. A secondary objective was to compare cross sections for molecular targets with those for atomic targets to investigate the applicability of a commonly employed additivity rule.

The organization of this thesis is as follows: Chapter II describes the experimental aspects of this study, including the beam preparation and selection, the gas targets, the gas

cell, the pressure regulation system, and the detection system. The methods used to analyze the data and to obtain the cross sections are given in chapter III. Details of the data analysis and the results are given in chapter IV. First, the dependence of the electron loss cross-section on target atomic number is discussed for the noble gases. Then the dependence of the loss cross section on the number of electron removed (Δq) from the projectile is discussed. A semiempirical method based on the independent electron approximation (IEA)[40,41] is presented for the purpose of establishing a systematic mean of estimating electron loss cross section. Finally, the electron loss cross sections for molecular targets are presented and the applicability of additivity rule is examined.

The conclusions are presented in chapter V.

CHAPTER II

EXPERIMENTAL SETUP

In this chapter, experimental details concerning the beam preparation and the gaseous targets will be discussed. Then the detector system and data acquisition procedure will be described.

A. Beam line

A 6 MeV/amu beam of Xe^{18+} was extracted from the K500 Superconducting Cyclotron and directed through a 22^o bending magnet, to remove ions with charges other than 18+, into the target chamber. Details of the experimental arrangement for the valves, chambers, collimators, gas cell, pumps, disperse magnet and detector is shown in figure 2. The target (front) chamber was located 10 m down-stream from the 22^o bending magnet. As shown in the figure 2, hand valve 1 isolated the front chamber from the cyclotron beam line. Also, by closing hand valve 4, the back chamber could be isolated from the front chamber.

The beam was focused by adjusting the upstream quadrupole magnets while viewing the beam spot on a phosphorescent screen positioned at the back of the target chamber via a closed circuit TV monitor. The gas cell was not placed in its position until after the focusing was completed.

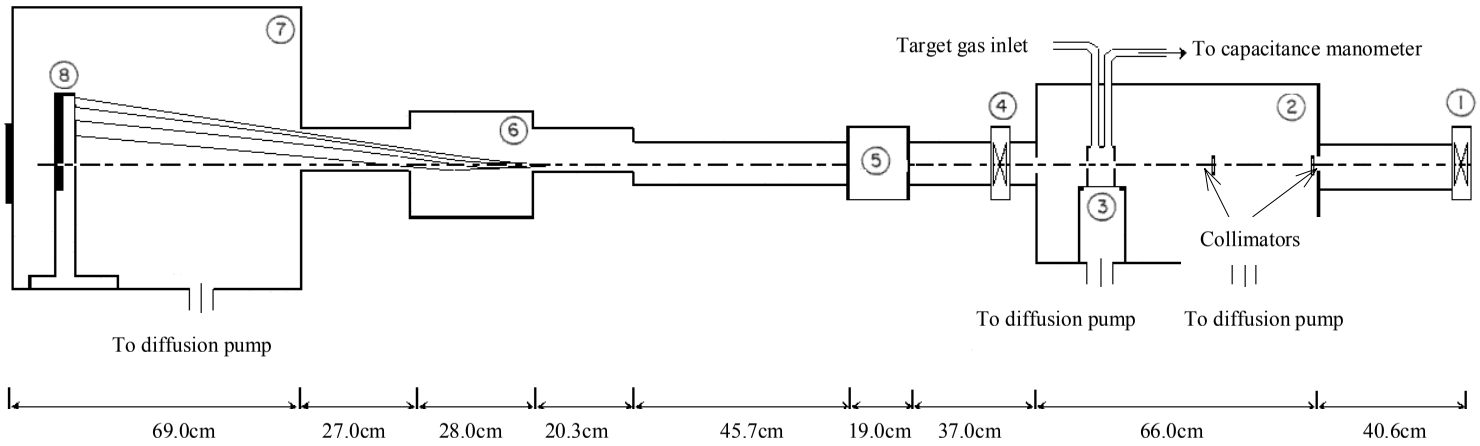

1 manual valve
2 front chamber
3 gas cell
4 manual valve
5 turbo pump
6 charge dispersion magnet
7 back chamber
8 position sensitive microchannel plate detector

Figure 2. Schematic diagram of experimental setup.

Inside the target chamber, the beam passed through two collimators of diameter 1 mm and 2 mm, respectively before entering the outer cylinder of a windowless gas cell. The outer cylinder of the gas cell had a 1-mm entrance aperture, which also acted as a third collimator (see figure 3). The cell was differentially pumped and had an effective length [23] of 2.08cm. Details of the gas cell system are described in section B. The pressure inside the gas cell was measured by a capacitance manometer and was held constant to within ±0.1 mTorr by a flow controller and an automated valve. The pressure controller compared the preset pressure setting with the manometer pressure and sent a feedback signal to the automated valve. Ion gauges were used to monitor the pressures in the beam line and front chamber, which varied between 1.5×10^{-6} and 5.0×10^{-6} Torr, depending upon the gas cell pressure and vacuum history. After exiting the gas cell, the beam passed through a charge dispersing magnet and on into a 1-D positive sensitive, microchannel plate detector (PSD). Details of the detector are described in section C. The detector could be moved up and down on a motor driven mount in order to optimize the separation between charge states. To avoid rate-dependent gain changes and extraneous peaks due to pulse pile-up, the beam intensity was kept between 1000 and 1500 counts/s. The charge distributions were counted until the statistics in the four-electron loss peak was better than 2%.

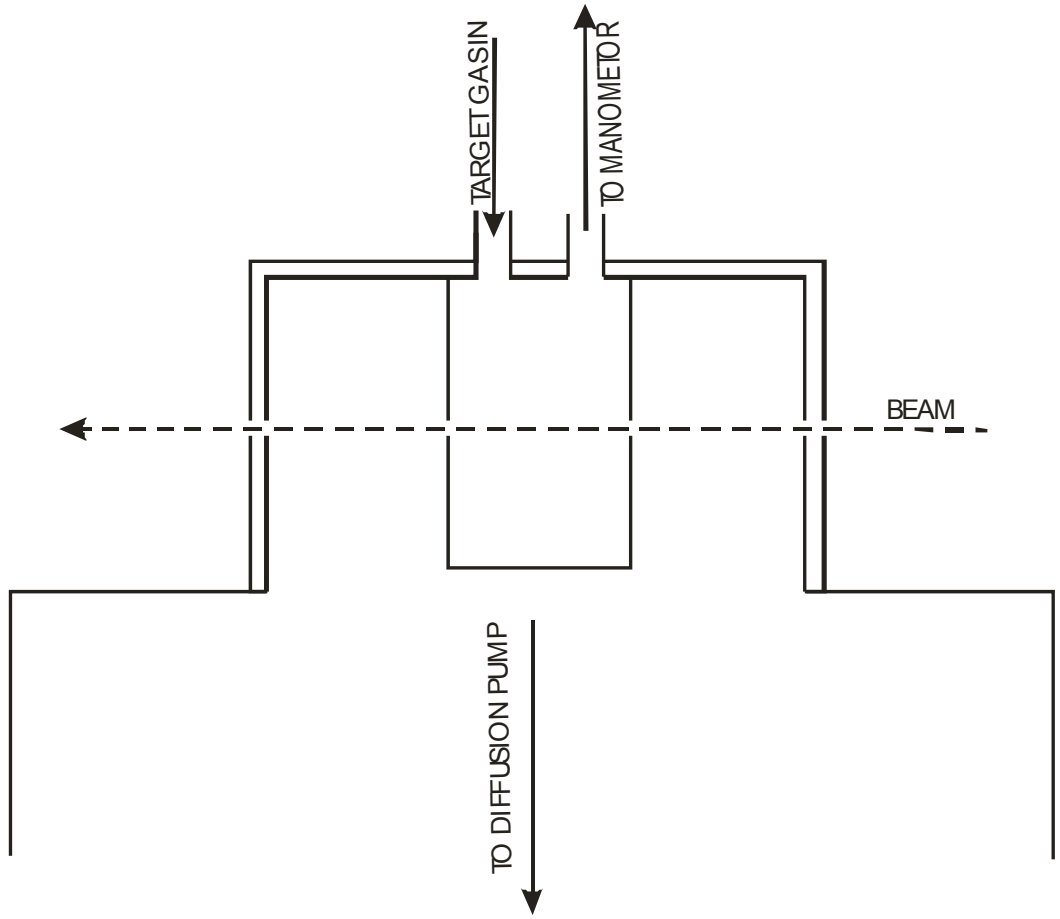

Figure 3. Schematic diagram of differentially pumped gas cell.

B. Gaseous targets

The target Z-dependence of electron loss was investigated using the noble gases He, Ne, Ar, Kr, and Xe. The question of cross section additivity was explored using the molecular gases listed in table I. Also tabulated are the atomic number, average atomic number and the pressure range employed. Special caution was taken when using silane because of its explosive properties when exposed to air.

Table I. The pressure (mTorr) range and the atomic number or average atomic number of the target gases

Gas	Pressure range	Atomic or average atomic number
H_2	0-200	1.00
He	0-200	2.00
CH_4	0-64	2.00
C_3H_8	0-64	2.36
SiH_4	0-64	3.60
CO	0-64	7.00
N_2	0-64	7.00
CO_2	0-64	7.33
O_2	0-64	8.00
C_3F_8	0-64	8.18
CF_4	0-64	8.40
SF_6	0-64	10.00
Ne	0-64	10.00
Ar	0-64	18.00
Kr	0-64	36.00
Xe	0-64	54.00

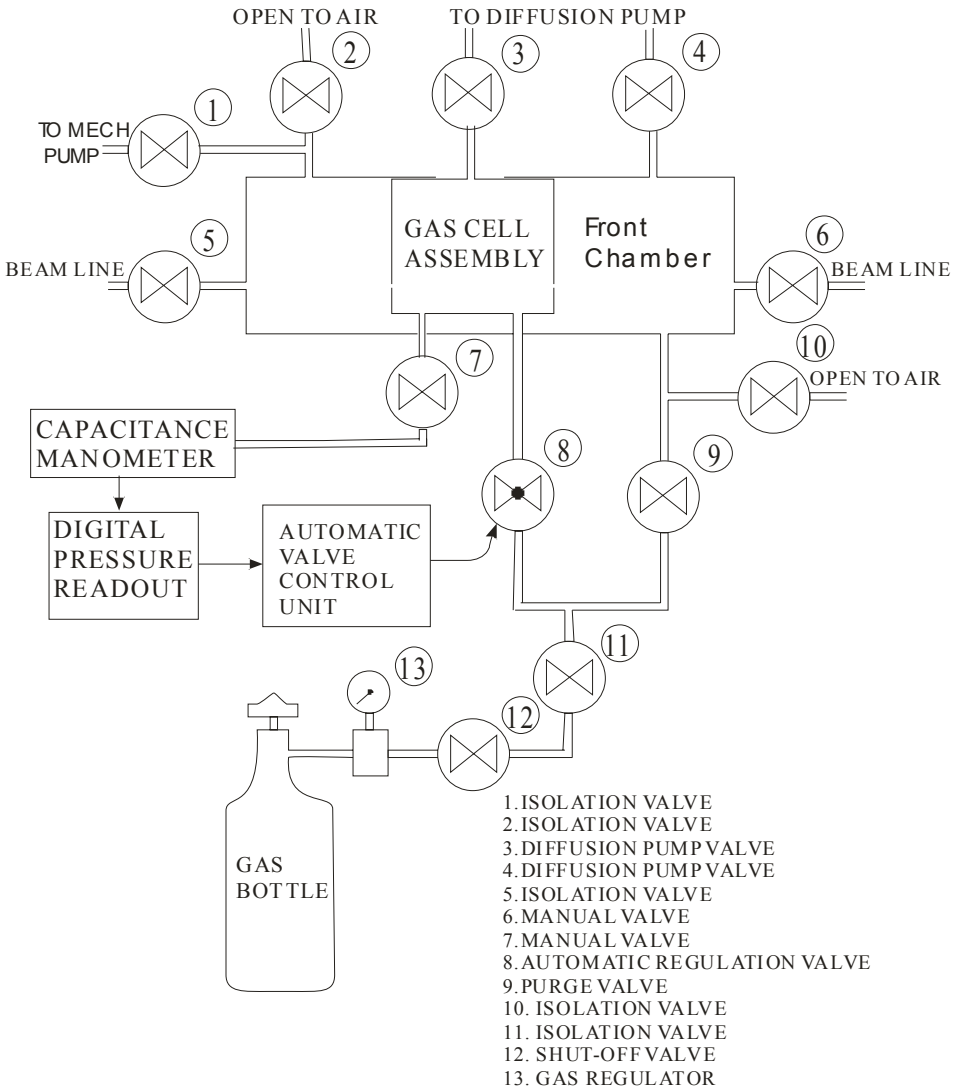

Figure 4. Target gas manifold system. The pressure in the gas cell was regulated by the automatic flow valve 8 which was controlled by the MKS pressure/flow controller by comparing the pressure signal from the capacitance manometer with the preset pressure.

1. Gas Cell

The gas cell assembly used in the present experiment consisted of an outer cylinder to limit the gas flow into the vacuum chamber and an inner cylindrical gas cell, as shown in figure 3. Obviously the effective path length in the gas cell is longer than the physical path length because of the gas streaming from the apertures as the result of differential pumping. It was estimated that the effective path length was 2.08 cm and the diameters of the entrance and exit apertures of the gas cell were 2 mm. Differential pumping maintained the pressure in the vacuum chamber from1.0 to 5.0×10^{-6} Torr with gas cell pressures ranging from 0 to 300 mTorr. The effective thickness π of the target cell is given by the following equation:

$$\pi = \rho \ell \tag{2-1}$$

where $\rho = \frac{\alpha N_A P}{RT}$

In the above equations, l is the effective length of the gas cell in centimeter, ρ is the gas atom density in atoms/cm^3, P is the measured pressure in atm, α is the number of atoms per molecule, N_A is Avogadro's number, R is the gas constant (0.08206 $\frac{L-atm}{mol-K}$), and T is the temperature in K.

2. The target gas handling system

The target gas handling system is shown in figure 4. The gas cell pressure was maintained by regulating the gas flow with an automatic valve (valve 8). Generally, a pressure control system consists of three basic parts (a) the pressure sensor, (b) the

controller and control valve and (c) the system whose pressure is to be controlled. The pressure sensor was the Baratron Absolute Pressure Transducer (MKS Co. Type 627B), which provided repeatable pressure measurements in the range from 1000 Torr to as low as 0.02 Torr full scale. It was connected to the gas cell through a steel pipe and manual valve 7. The sensor provided 0 to 10 VDC output that was linear with pressure and independent of gas composition. By comparing the pressure signal from the Baratron with the pre-set pressure, the controller automatically adjusted the flow rate into the gas cell via the control valve 8 to maintain the desired pressure. The pressure could be held constant to within ±0.6% over the 20 minutes time period of a typical measurement.

Manual valves 5 and 6 were used to isolate the front and back chambers, respectively from the cyclotron vacuum system. The pump down procedure was described as follows: first, valve 1 was slowly opened (all the other valves initially were closed) and the mechanical pump started to rough the system down to approximately 1×10^{-3} Torr, at which point manual valves 3 and 4 to the diffusion pumps, were opened. Then valve 1 was closed immediately. Finally, manual valves 5 and 6 were opened after the front chamber pressure dropped below 1×10^{-5} Torr, and then valve 7 was opened. The reverse procedure was used to vent the chamber.

During the experiment, the pressure at the output side of the pressure regulator (13) was set at 5 psi.

When changing from one gas to another, the following procedure was used. First, valve 8 was closed. After attaching a new gas bottle and regulator, the tygon tubing to

valve 11 was disconnected and flushed by flowing same of the new gas through it for few seconds. Then the tygon tubing was quickly reconnected to valve 11. The pressure at valve 12 was adjusted to 5 psi. Next, valve 11 was opened to allow gas to enter as for as valves 8 and 9. Then valve 11 was closed and pumped out by slowly opening valve 9. The last two steps were repeated several times in order to get all the residual gas out of the system. Finally, with valve 9 closed, valve 11 was fully opened and the system was ready for operation.

C. Detector system

1. Position Sensitive Microchannel Plate Detector (PSD)

A Position Sensitive Microchannel Plate Detector (PSD) was used to measure the relative intensities of the different charge states of Xe ions. A schematic diagram of a microchannel plate, illustrating its principle of operation is shown in figure 5 [24 and references therein]. Microchannel plates are leaded-glass discs that contain millions of tiny pores etched into them. The pores are typically 8-25 micrometers in diameter, 10-40 micrometers center to center and 40-100 times longer than their diameter. The inner surface of each pore is coated with lead-oxide (PbO) glass that will readily release multiple secondary electrons when a single incident particle (ion, electron, photon etc.) enters the channel and ejects an electron from the channel wall. One enlarged channel in figure 6 shows the principle of its gain. In the present application, two MCPs were stacked one on top of the other to form what is called a chevron array .The top surface of the top MCP, called the cathode, was held at a negative voltage of around -1800 v and the bottom surface of the bottom MCP, was held at approximately -300 v. Having negative charge at the cathode, the electrons ejected within the MCP are accelerated towards the positively charged anode. Secondary electrons are also accelerated by the electric field.

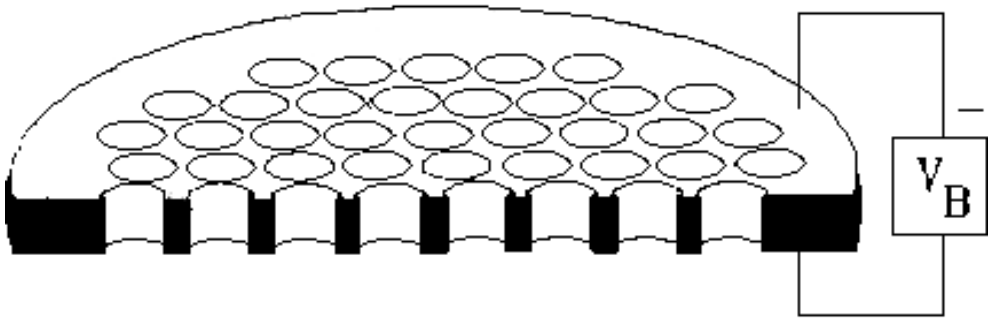

Figure 5. Illustration of the structure of a Microchannel plate (MCP) **[24]**

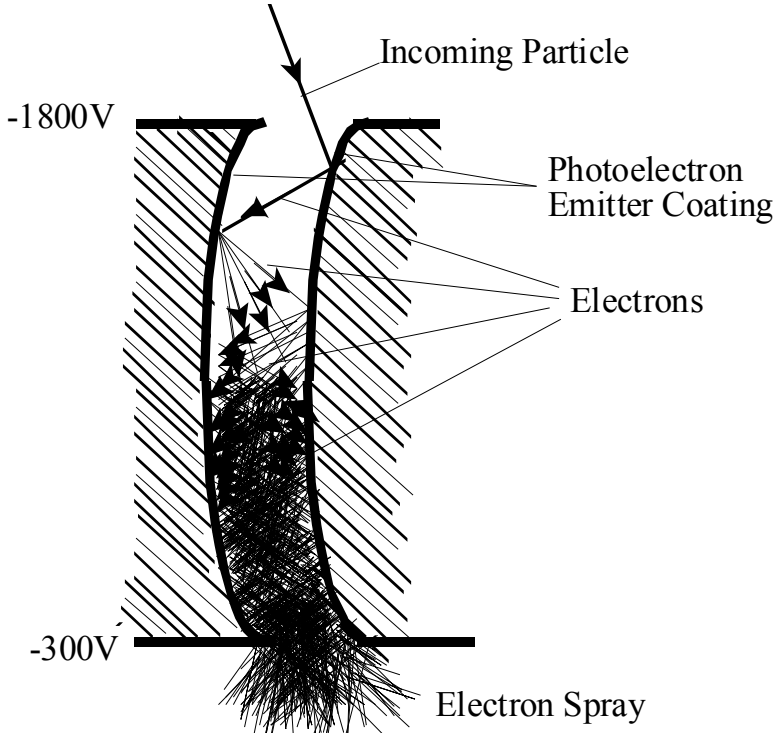

Figure 6. An enlarged view of one channel of the MCP and the principle of its gain.

The secondary electrons travel along their parabolic trajectories until they strike the channel surface, thus producing more secondary electrons. This process is repeated many times along the channel; as a result, this cascade process yields a cloud of several thousand electrons, which emerge from the rear of the plate. The upper surface is coated with a semiconductor photocathode material that also penetrates slightly into each pore to improve the efficiency of the device. When two or more MCPs are operated in series, a pulse of 10^8 electrons is generated by a single particle input.

The PSD shown in figure 7 is composed of two MCPs having an active length of 10 cm and width of 1.5 cm which are stacked with the angles of the channels oriented opposite each other. As will be explained in the coming section, the position of impact of the incident Xe ion was determined by comparing the top signal with the bottom signal of the PSD. The detector could be moved up and down in order optimize the separation of adjacent charge states.

2. Data acquisition

The amount of charge collected at each end of the resistive anode is proportional to the distance the charge must travel (i. e., the resistance associated with the path length through the anode). Therefore, the position of the incident particle may be determined by comparing the amplitude of the corresponding signal appearing at the top and bottom of the resistive anode. The electronic components used to accomplish this task are shown schematically in figure 7. Both the bottom and top signals from the resistive anode were amplified by preamplifiers and then fed to spectroscopy amplifiers (Ortec 571 or 572).

The amplified signals were added and the sum signal inverted by a Dual Sum & Inverter unit (Ortec 433A). The top signal and the sum signal were then sent to a position sensitive detector analyzer unit (Ortec 464). This unit produces an output signal that is proportional to the position of the incident particle on the PSD by taking the ratio of the top signal to the sum signal. The position signals were analyzed by a personal computer based multichannel analyzer system (Oxford model PCA3) and the resulting charge distribution spectra were recorded on disk.

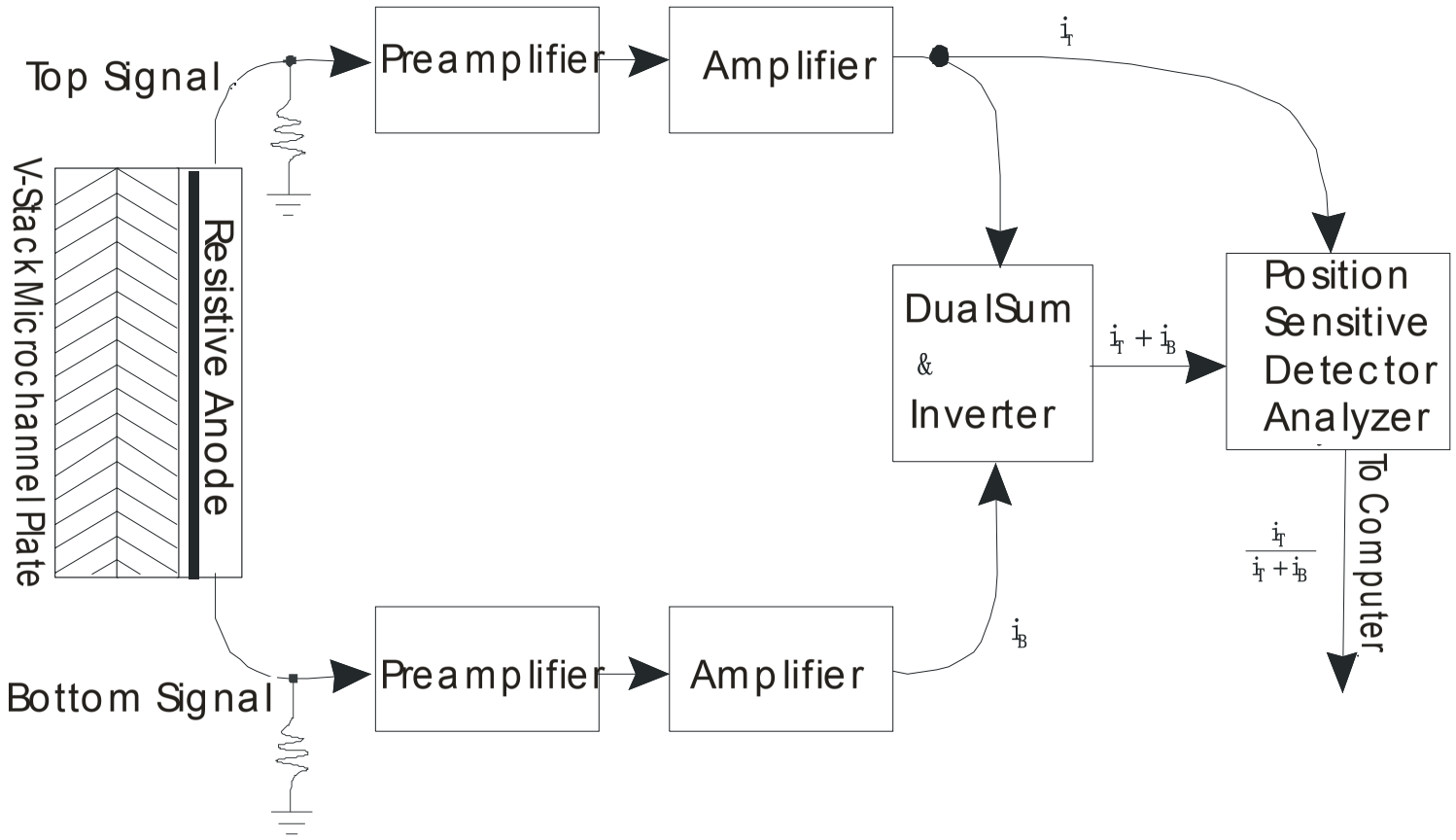

Figure 7. Schematic diagram of electronics for data analysis. The position was determined by comparing the top signal to the sum of the top and bottom signals.

CHAPTER III

DATA ANALYSIS METHODS

In this chapter, the growth curve method [24] and an approximate solution to the rate equation will be described. Then the method used to determine cross sections for specific charge states will be discussed.

A. Charge distribution and growth curves

When a high energy particle of charge q passes through a gaseous target, its charge may increase or decrease as a result of electron loss or capture. Generally, these charge changing processes can be represented as:

$$P^i + T = P^f + T^{f'} + (f + f' - i)e\,,$$

Where P represents the high energy projectile with initial charge i and final charge f; T represents the neutral target with final charge f'; $(f + f' - i)e$ is the number of electrons released in the collision.

In order to completely describe the collision, it would be necessary to measure the charges of the incident particle and the target before and after the collision and to determine the momenta of the released electrons. However, this kind of experiment is generally too difficult to perform for a complex (many electron) collision. In the present work, the much simpler task of determining cross sections for single and multiple

electron loss from the projectile is undertaken. Specifically, the dependence of electron loss by 6 MeV/amu Xe^{18+} on target atomic number and composition was studied.

After passing through the target gas cell, a incident beam contains ions in many charge states. However, if the target is quit thin, the incident charge state still dominates. A typical charge spectrum of projectile ions, detected using the one dimensional position sensitive microchannel plate detector (MCP-PSD), is shown in figure 8. This figure shows that a) the charge state of incident beam still dominates; b) the probability of electron loss is much lager than that of electron capture, and c) as many as twelve electrons may be lost in a single collision. In figure 8, the dominant main peak is due to the charge unchanged Xe^{18+} beam. Positive numbers indicate the charge states of the projectile after passing through the gas cell. Each charge state peak appearing in the spectrum was integrated and divided by the total number of incident ions to obtain the corresponding charge fraction F_i of projectile ions in charge state i. For most of the targets, the charge state fractions were measured at pressures of 0, 1, 2, 4, 8, 16, 32 and 64 mTorr. In the hydrogen and a helium target measurements, pressures up to 300 mTorr and 200 mTorr, respectively, were employed because of their lower densities. The 0-mTorr spectrum is used to determine the contributions to the various charge states from stripping in the beam line residual gas. The rate of change of charge fraction F_i as the projectile traverses a gas cell of effective length l cm containing gas atom density ρ cm^{-3} is given by the differential equations:

$$\frac{dF_i}{d\pi} = \sum_k F_k \sigma_{ki} - F_i \sum_j \sigma_{ij} \qquad (3\text{-}1)$$

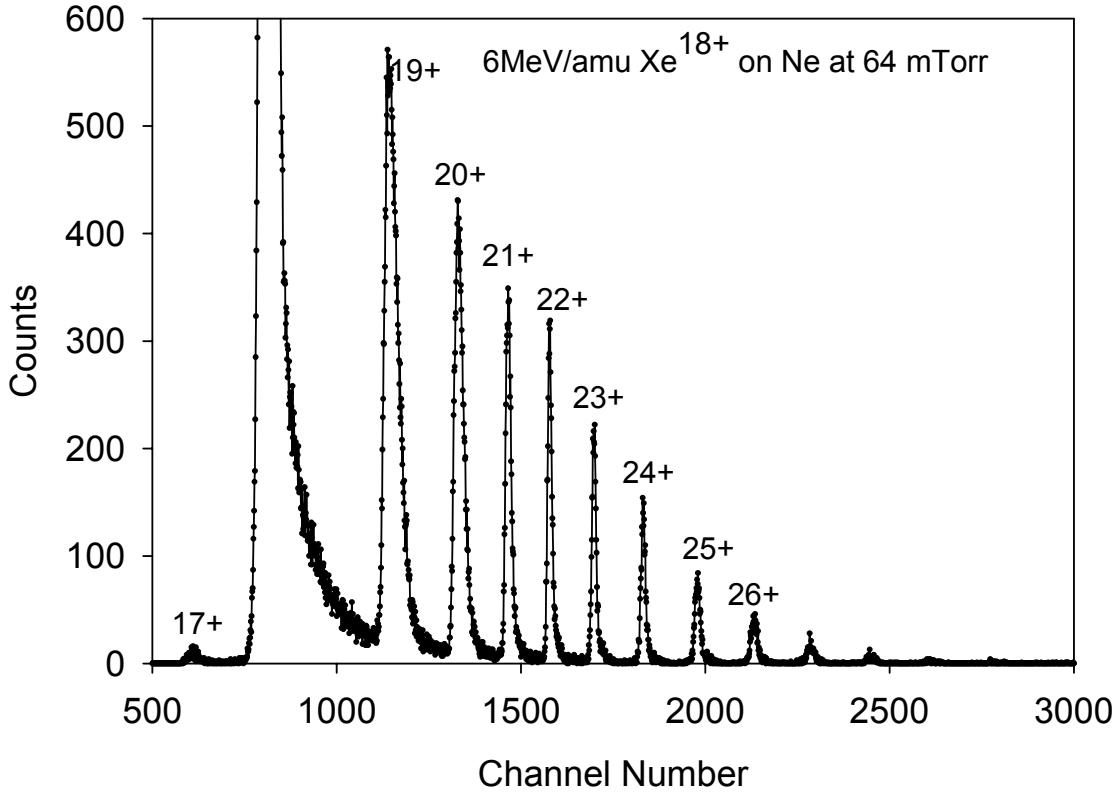

Figure 8. Typical position spectrum of the outgoing projectile charge distribution. The probability of electron loss (q>18+) is much larger than that of electron capture (q<18+). The percentage of charge changed beam is less than 25% of the incident beam.

In equation (3-1), $\pi = \rho l$ and σ_{ki} represents the cross section for changing from charge state k to charge state i by either capture (k>i) or loss (k<i) of electrons while σ_{ij} represents the cross section for changing from charge state i to charge state j by either loss (j>i) or capture (j<i) electrons. The first summation represents the rate of increase of the fraction of ions in charge state i via transformations from all the other possible charge states k, while the second term represents the rate of decrease of the fraction of ions in charge state i via transformations into all other possible charge states j.

The solutions to the set of coupled equation 3-1 are rather complicated, but for low enough pressures ($\sigma_{mn}\pi << 1$), they may be approximately represented by the following polynomials [25]:

$$F_i = a + b\pi + c\pi^2 + \cdots \quad , \tag{3-2}$$

where

$a = F_i$ when π=0

$b = \sigma_{qi}$ (cross section for changing from incident charge q to charge i in a single collision)

c = products of cross sections for producing charge state i in double collisions.

The first term in equation (3-2) is the background fraction of ions with charge state i (i.e., the fraction of incident ions that change to charge state i as a result of collisions with the residual gas in the beamline when there is no gas in the gas cell). In the pressure range employed, higher order terms (greater than 2) representing contributions from

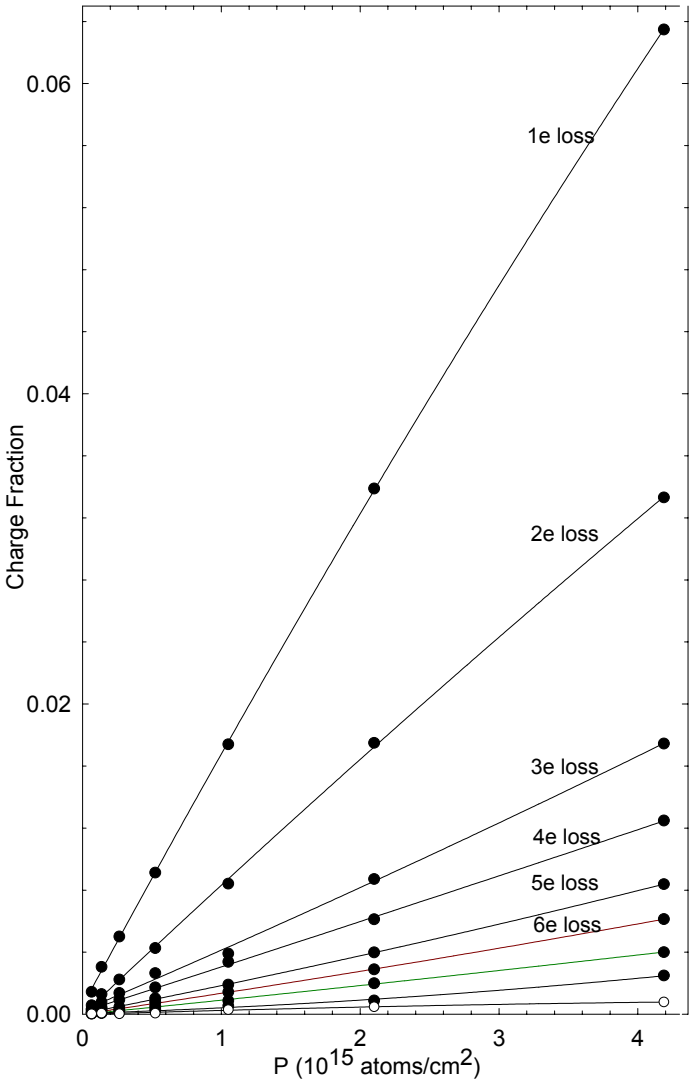

Figure 9. Charge fractions for 6 MeV/amu Xe^{18+} plotted as a function of Ne target thickness. Solid lines and filled circles are for electron loss. Dashed line and open circles are for electron capture. The lines show the results of least squares fits of equation 3-2 to the data In the low pressure region, the charge fractions vary linearly with target thickness, but at the higher values of π , substantial deviations from linearity are observed.

more than two collisions are expected to be negligible. Figure 9 shows typical growth curves of charge fractions vs. π (target gas thickness). These curves exhibit substantial deviations from linearity at the high target thicknesses.

B. Cross section determination

In the present application of the growth curve method, the charge fractions were measured over a range of pressures and plotted as a function of target thickness (π). Then second order polynomials were fit to these data. According to equation (3-2), the cross sections σ_{qi} are given by the coefficients of the linear terms.

Two fitting procedures were employed in the data analysis. In the first procedure, second order polynomials were fit to the charge fractions without first correcting them for charge changing collisions with the residual gas in the beam line. Presumably, this contribution is automatically accounted for by the parameter a in equation (3-2). The second fitting procedure was applied to charge fractions that had first been corrected for residual gas collisions. The charge fraction corrections were accomplished by subtracting the normalized zero pressure spectrum from each of the spectra measured at the other pressures to explicitly correct for the residual gas background. Fits to the corrected charge fraction vs. target thickness data sets were then made with the additional restraint that a=0. The results of both types of analyses for the eight electron

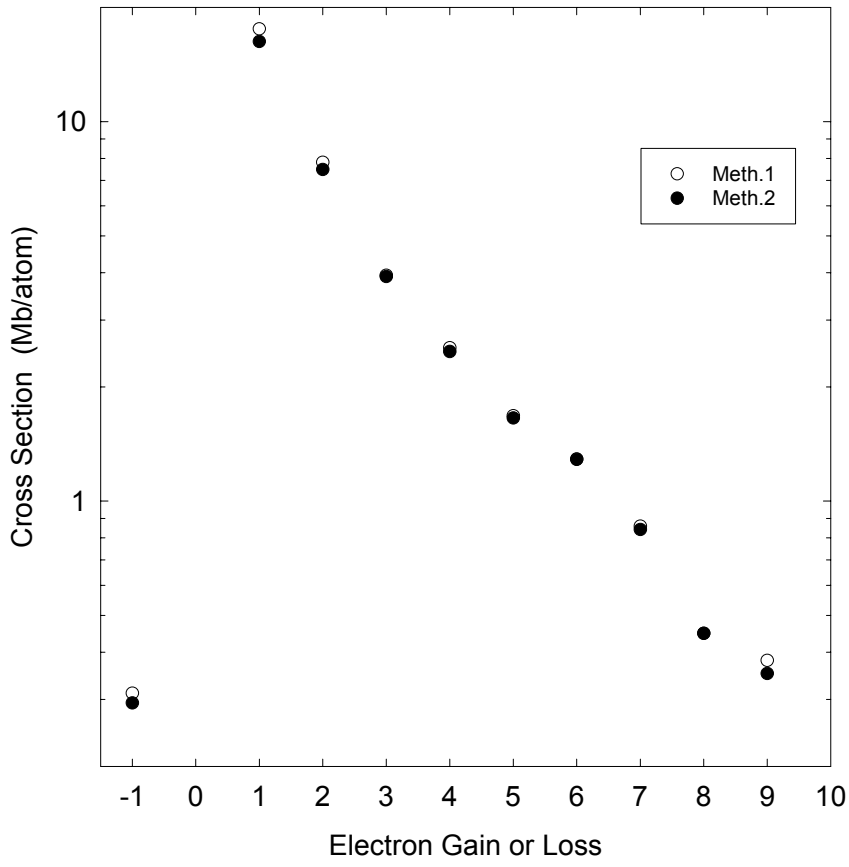

Figure 10. Comparison of the cross sections obtained for 6 MeV/amu Xe^{18+} ions in Ne using the two fitting procedures: with residual gas contribution subtracted (open circles) and without residual gas contribution subtracted.

loss peaks measured with a Ne target are shown in figure 10. The uncertainty in the cross section due to statistical errors is less than 1%, which is much smaller than the

uncertainties associated with the peak integrations and the effects of the background. Agreement of the cross sections determined by the two methods of treating the background is quite good.

Errors in the cross sections are due to uncertainties in (a) the effective length of the gas cell (2%), (b) the pressure measurements with the capacitance manometer (5%), (c) counting statistics, (d) efficiency nonuniformity of the PSD, and (e) peak integration. These uncertainties were taken into account along with the relative uncertainty of the fitting parameter b to obtain the absolute uncertainty in the cross sections, which was typically less than 15%.

The validity of the approximation involved in representing the thickness dependence of the cross section by a second order polynomial was tested by assuming a reasonable set of charge changing cross sections and calculating the growth curves for one to eight electron loss and one to three electron capture via numerical solution of the rate equations (equation 3-1). Then the calculated growth curves were fit with second order polynomials over the pressure range of zero to 100 mTorr and the cross sections obtained from the fits were compared with the assumed cross sections. In the case of electron loss, the largest difference between the value of the linear coefficient of the polynomial fit and the corresponding (assumed) cross section was 6%, which occurred for the one-electron loss case. The deviations for all of the multiple loss cross sections were less than 1%. In addition, it was found that the agreement improves rapidly as the pressure range is decreased. For larger pressure ranges, good agreement is obtained by increasing the polynomial to third order.

CHAPTER IV

RESULTS AND DISCUSSION

In the first part of this chapter, the electron loss cross sections for 6 MeV/amu Xe^{18+} ions on noble gas targets are presented and discussed. A semiempirical scaling procedure based on the IEA is described. Then the results of the electron loss cross section measurements for molecular targets are presented. Based on these results, the applicability of an additivity rule is discussed in the second part of this chapter.

A. Target Z-dependence of electron loss by 6 MeV/amu Xe^{18+}

Many investigators have put forth considerable effort to study the charge changing cross sections for electron capture and electron stripping by high energy particles in collisions with target atoms or molecules. Because of the complexity of the charge changing phenomena, theoretical methods must resort to various assumptions and simplifications when applied to multiple electron processes. Among these theoretical methods [reference 13 and references therein, 26-29], Bohr's method [28-29] is well known and it states that if the distance of closest approach in a collision is much smaller than the atomic radius, the collision can be viewed as a collision between a bare nucleus and free electrons. Bohr's theory predicts that the electron loss cross section of both light and heavy projectiles on a light target is a quadratic function of the target atomic number.

Whereas in the case of a heavy ion collision with a heavy target, a dependence on $Z_2^{1/3}$ is predicted. However, the present study shows that the electron loss cross section is a linear function of Z_2 in both regimes. Details of the linear relationship will be discussed in the following sections.

1. Cross sections for collisions with noble gas targets

By using the methods described in chapter III, the capture and loss cross sections of 6 MeV/amu Xe^{18+} ions in the noble gases were determined and their values are listed in table II. The entries listed for $\Delta q \geq 9$ (Ne through Xe) were determined from composite growth curves constructed by summing the charge fractions of all statistically significant peaks in the charge distribution above that of $\Delta q = 8$. The one electron capture peak was statistically significant for all of the targets except H_2 and He. Approximately 8 and 13 statistically significant loss peaks were observed for targets whose average atomic numbers were less than and greater than 8, respectively. The exception was for He, which had only 5 significant loss peaks. The measured electron loss cross sections for noble gas targets also are shown as a function of the number of electrons removed from the projectile (Δq) in figure 11.

Table II. Experimental electron capture and loss cross sections for 6 MeV/amu Xe^{18+} colliding with noble gas targets. Except for helium, individual cross sections were measured for the loss of as many as eight electrons. Those cross sections for which the projectile lost more than 8 electrons were combined together and are listed under the heading >8.

		He	Ne	Ar	Kr	Xe
Radius(Å)		0.49	0.51	0.85	1.00	1.20
Atomic number		2	10	18	36	54
		Cross sections(Mb)				
Capture 1 e		0.010 ±0.00	0.26 ±0.06	0.22 ±0.05	0.22 ±0.05	0.07 ±0.07
Loss Cross Sections	1	3.0 ±0.3	16 ±1	24 ±2	27 ±3	34 ±3
	2	1.6 ±0.2	7.8 ±0.7	11 ±1	13 ±1	15 ±1
	3	0.19 ±0.02	3.8 ±0.4	5.6 ±0.5	7.2 ±0.7	9.0 ±0.9
	4	0.08 ±0.01	2.9 ±0.3	4.1 ±0.4	5.3 ±0.5	6.7 ±0.6
	5	0.021 ±0.003	2.0 ±0.2	3.2 ±0.3	4.5 ±0.4	5.6 ±0.5
	6	0.010 ±0.001	1.3 ±0.1	2.7 ±0.3	3.8 ±0.4	4.7 ±0.5
	7	0.0044 ±0.0008	0.85 ±0.09	2.5 ±0.3	3.5 ±0.4	4.6 ±0.5
	8		0.47 ±0.06	1.8 ±0.2	3.1 ±0.4	3.8 ±0.5
	>8		0.33 ±0.05	2.2 ±0.3	7.3 ±0.6	12 ±2
Total loss		4.9 ±0.3	35 ±2	56 ±3	75 ±3	95 ±4
$Z_{2(eff)}$		2.0	5.9	7.8	9.1	10.4

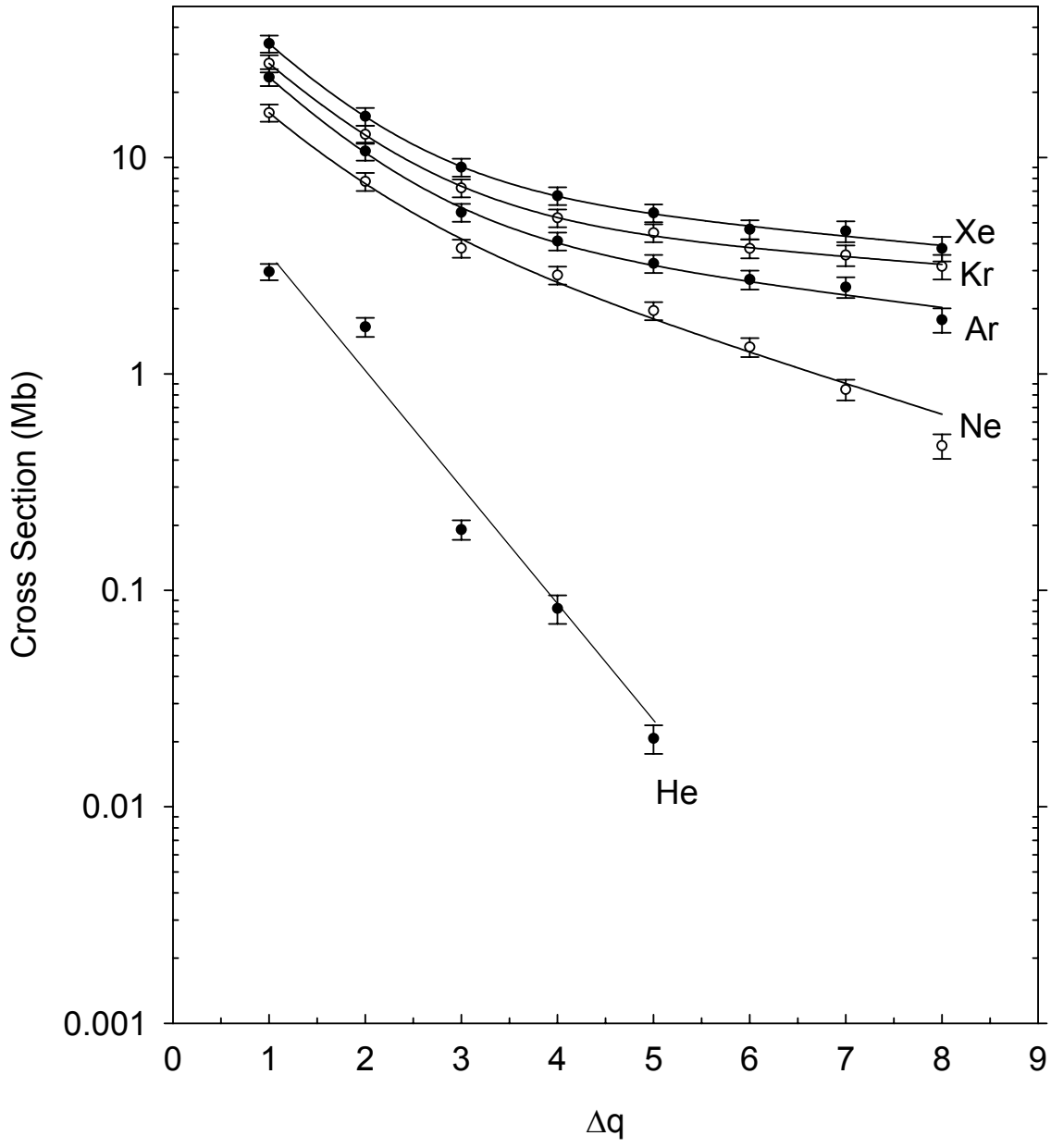

Figure 11. Single and multiple electron loss cross sections plotted as a function of the number of electrons removed from the incident 6 MeV/amu Xe^{18+} ions. The solid lines were fit to the points using two exponential functions except for He, where only one exponential function was used.

2. Dependence of electron loss cross sections on Δq

In Fig 11, the cross sections for the He target are reasonably well represented by a single exponential function (solid line), whereas the cross sections for the other targets display a dependence on Δq that requires two exponential components to describe. This is because the rate of decrease in cross sections for $\Delta q \geq 4$ as a function of Δq slows dramatically with increasing target atomic number. The second exponential component may reflect the effect of Auger decay, which should become an increasingly important mechanism for electron loss as electrons are removed from inner shells in high multiplicity (i.e., small impact parameter) collisions

3. Z-dependence of the total loss cross sections

The total electron loss cross section is defined as the sum of the individual electron loss cross sections ($\sigma_{total} = \sum_{i=1}^{8} (\sigma_i)_{loss}$). As shown in figure 11, the individual electron loss cross sections decrease with the increasing Δq. The cross sections for one- and two-electron loss (σ_1 and σ_2) are much larger than the other electron loss cross sections. This is shown in figure 12 where the ratios $(\sigma_1 + \sigma_2)/\sigma_T$ and $(\sigma_T - \sigma_1 - \sigma_2)/\sigma_T$ are plotted as a function of target atomic number. Clearly, σ_1 and σ_2 are the dominant contributors to the total cross section. However, the one- and two- electron loss contribution decreases from around 80% for He to around 50% for Xe. This observation

points to the increasing importance of large multiplicity collisions as the target atomic number increases.

Figure 13 shows the dependence of the total electron loss cross section for 6 MeV/amu Xe^{18+} on target atomic number for the noble gas targets. The plot shows that the data appears to lie along two straight lines, with the He and Ne points defining a line having a relatively steep slope and the rest of the points defining a line having a significantly smaller slope. This behavior is remarkably similar to that observed by Alton *et al.* [19] for 0.36 MeV/amu Fe^{4+} ions and by Graham *et al.* [30] for 4.66 MeV/amu Pb^{54+} ions. Alton *et al.* also found that their measured one electron loss cross sections were well predicted by a dependence on $Z_2^{1/3}$. However, application of their formula to the present collision systems results in one-electron loss cross sections that are too small by a factor ranging from 1.7 for He to 8.5 for Xe.

The two lines shown in figure 13 intersect around atomic number 15. The total electron loss cross sections are given by the equations

$$\sigma_T = -2.194 + 3.689 Z_2 \qquad \text{for } Z_2 \leq 10 \tag{4-1}$$

and

$$\sigma_T = 36.72 + 1.076 Z_2 \qquad \text{for } Z_2 \geq 18 \tag{4-2}$$

with σ_T in units of Mb.

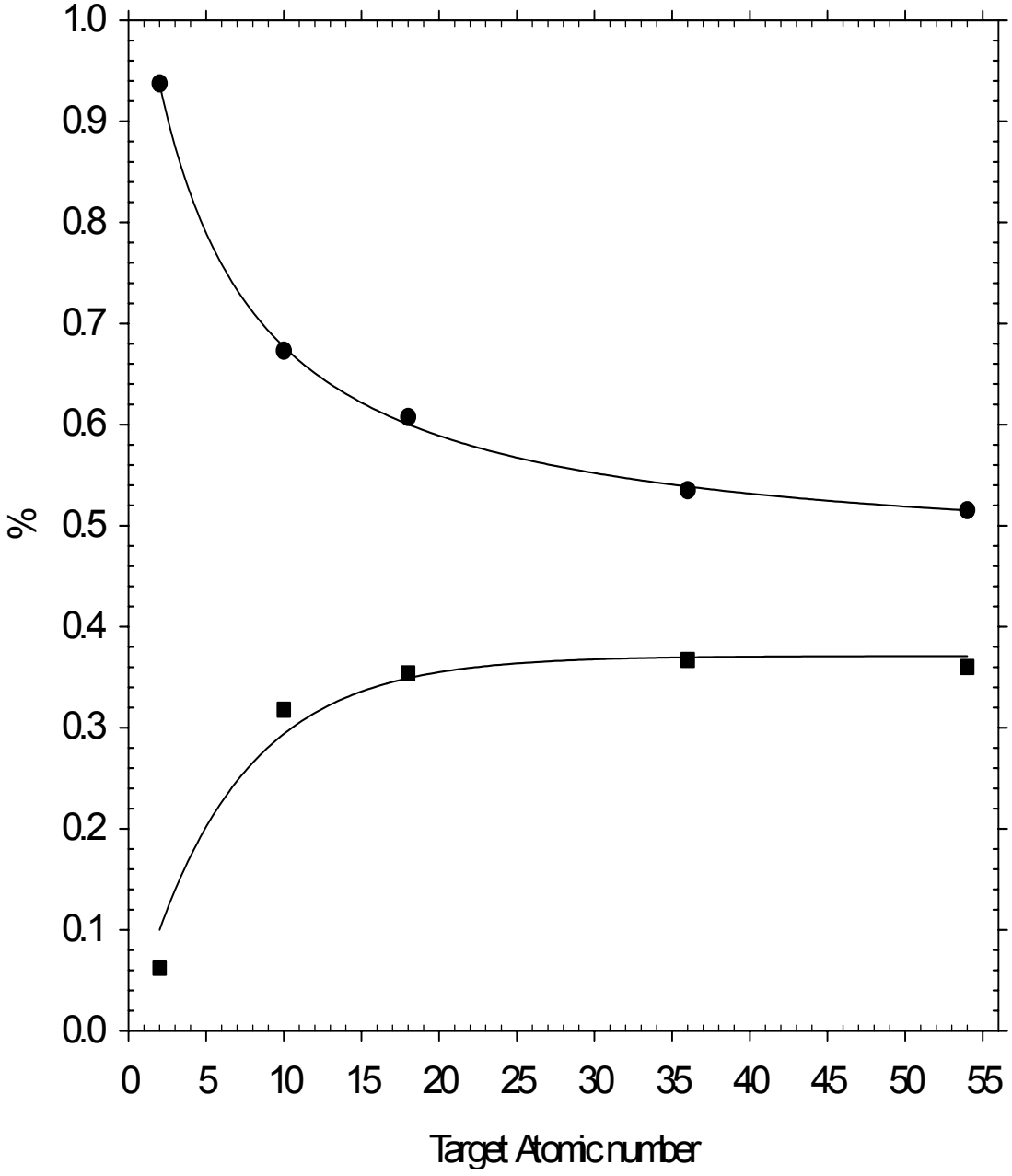

Figure 12. The cross section ratios $(\sigma_1 + \sigma_2)/\sigma_T$ (solid circles) and $(\sigma_T - \sigma_1 - \sigma_2)/\sigma_T$ (solid squares) plotted as a function of the target atomic number.

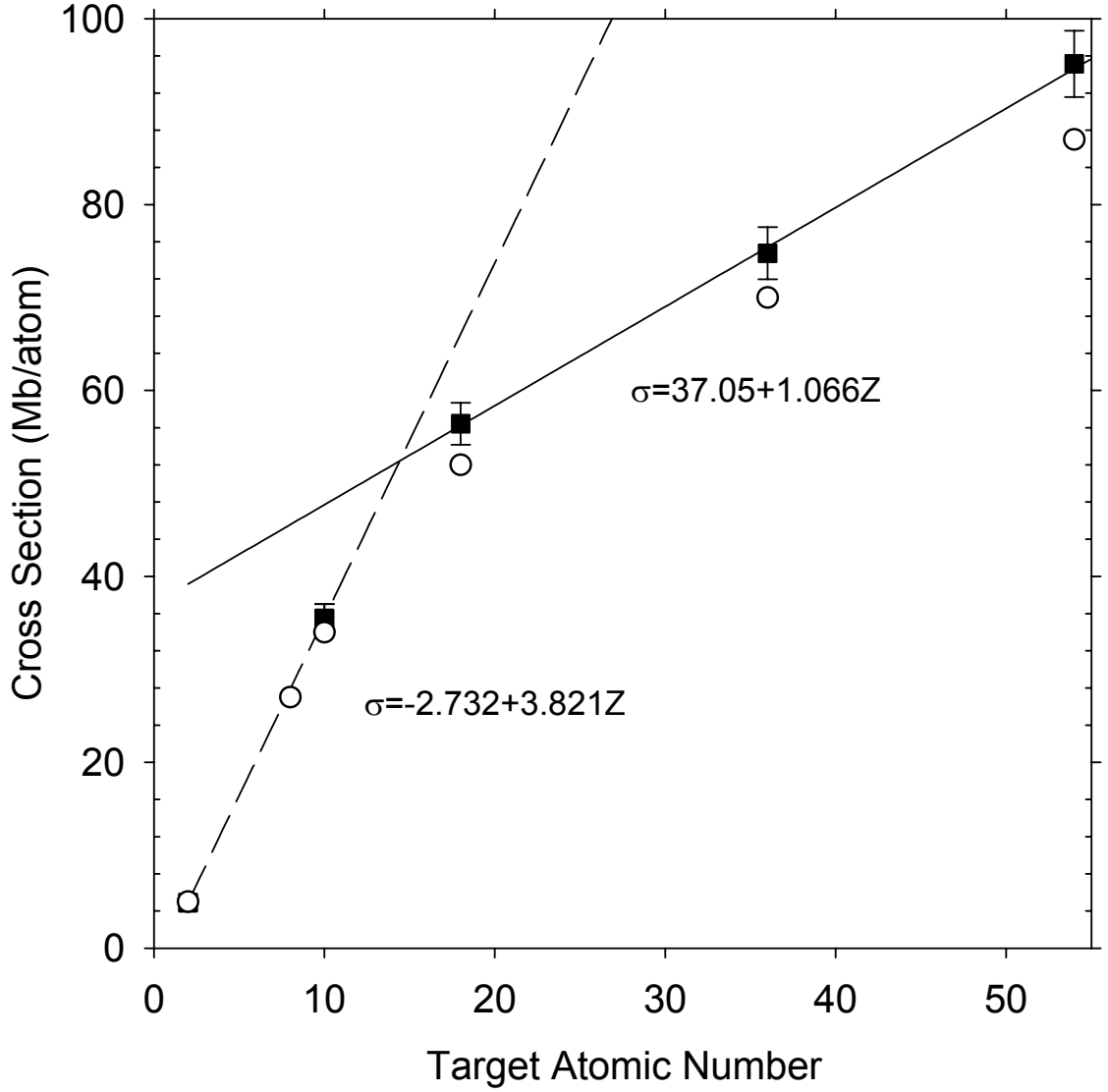

Figure 13. Total electron loss cross sections for 6 MeV/amu Xe^{18+} ions colliding with noble gas targets plotted as functions of target atomic number. The dashed line was drawn through the experimental data of helium and neon while the solid line was fit to the experimental data of Ar, Kr and Xe.

The results of n-CTMC calculations performed by Olson *et al.* [31] are also shown in figure 13. For these calculations, 18 electrons were centered on the Xe-ion in order to model the $3d^{10}4s^{2}4p^{6}$ electron configuration. The overall agreement with experiment is quite good and the slopes of the two straight line segments are accurately predicted. In applying the n-CTMC model, the actual ionization energy was assigned to each bound electron to account for the increasing ionization energies of the remaining electron as sequential stripping proceeds. After electrons are stripped, the actual ionization energy will increase. Therefore, the n-CTMC model may be considered to be an independent event model rather than an independent particle model. It also employed an energy deposition model to describe the high ionization stages. [32]

Generally, electron loss occurs as a result of (a) interaction between the projectile electron and the target electron (e-e interaction) and (b) interaction between the projectile electron and the target nucleus (e-n interaction). Therefore, the total electron loss cross section can be approximately expressed as:

$$\sigma_T \cong n_e \sigma_{e-e} + Z_2^2(eff)\sigma_{e-e} \tag{4-3}$$

where σ_{e-e} is the cross section for e-e interaction, n_e is the number of target electrons and $Z_2(eff)$ is the screened target nuclear charge. By assuming n_e and $Z_2(eff)$ for He are 2, and equating equation (4-3) to the measured total electron loss cross section, σ_{e-e} can be estimated. If we consider only interactions including the target outer shell electrons(i.e., take $n_{e\text{-}e}$ to be the number of target outer shell electrons), then

$Z_2(eff)$ can be estimated by equating equation (4-3) to the measured total electron loss cross sections. The results are listed in the last row of table II and are shown in figure 14.

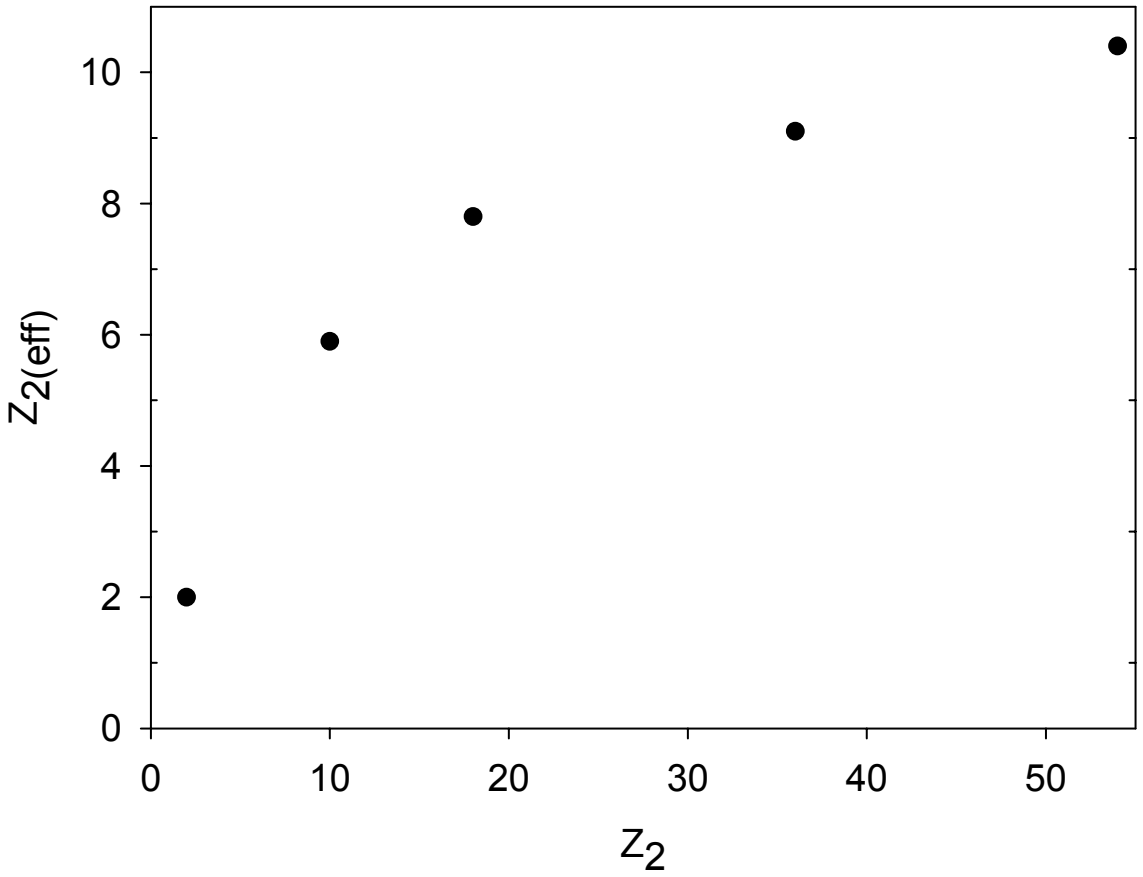

Figure 14. Effective charge ($Z_{2(eff)}$) of the noble gas targets as a function of atomic number.

It is evident that the trend of $Z_2(eff)$ is very similar to that of the total electron loss cross section shown in figure 13. The fact that the Ar, Kr, And Xe targets are more highly screened than the He and Ne targets suggests that the change in screening between Ne and Ar is responsible for the change in the slope of the Z-dependence exhibited by the data in figure 13.

4. Single electron capture

The single-electron capture cross sections for noble gas targets plotted as a function of Z_2 are shown in figure 15. The cross section for helium is much lower than the rest while neon gives the largest cross section. This low value of the cross section for He is probably attributable to both its low number of electrons and its relatively high electron binding energy. It is further noted that the capture cross section decreases above Z_2 =10. Interestingly, this observation is quite different from the theoretical predictions and experimental results for low Z_1 projectiles, which generally shows the capture cross section to increase with Z_2 when Z_2 is not large [33-39]. The capture cross section becomes almost constant when Z_2 tends to a large value [13]. The reason for the later observation is that capture follows a trend which is completely opposite to the loss, i.e. the higher the probability of electron loss, the lower the probability of electron capture and vice versa.

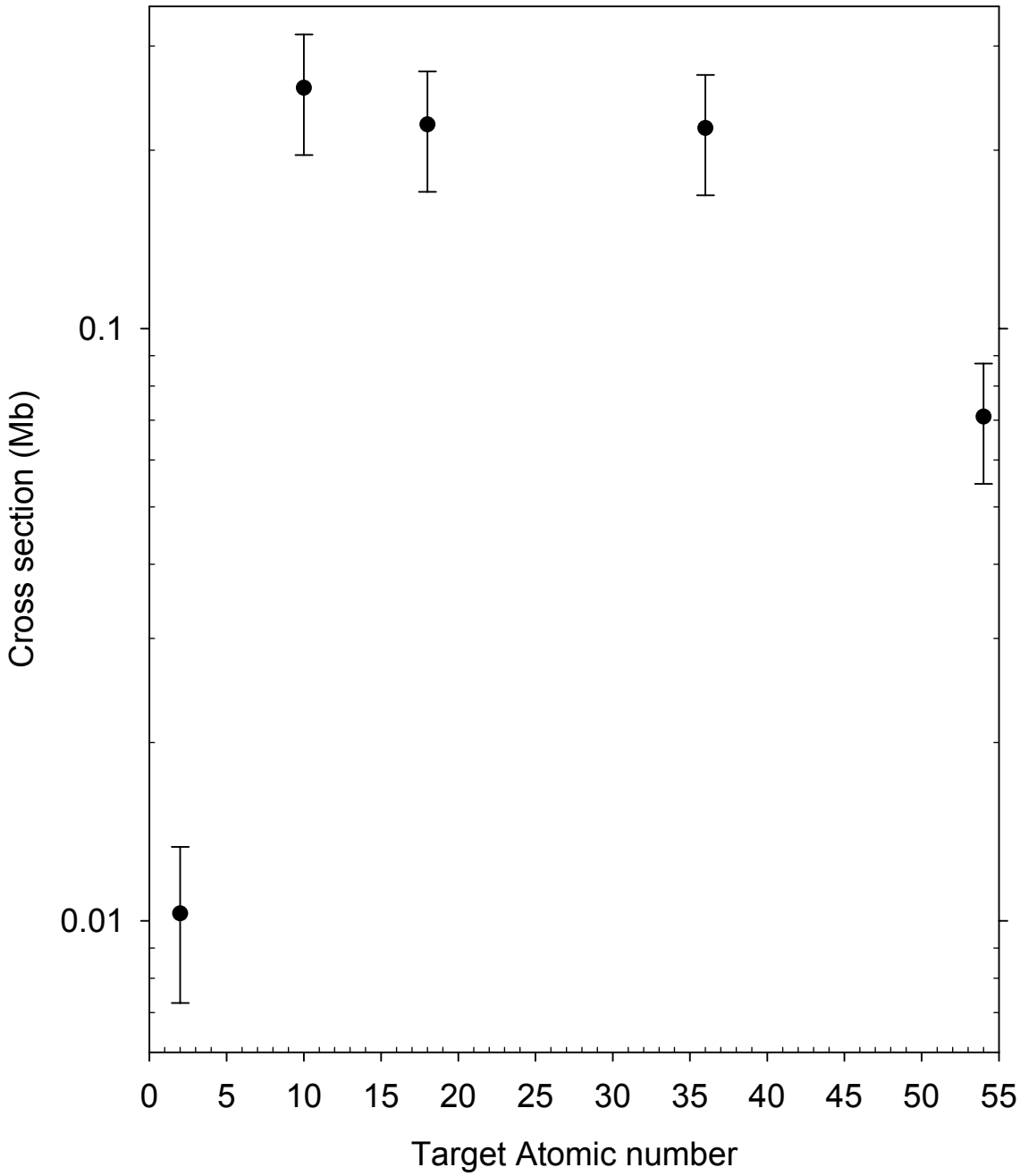

Figure 15. Cross sections for single-electron capture by 6 MeV/amu Xe^{18+} from noble gas targets as a function of atomic number.

5. Semi-empirical method for systematizing the $\sigma(\Delta q)$

As a mean of exploring the systematic dependence of the electron loss cross sections on Δq, a semi-empirical scaling method was developed by employing the IEA [40, 41] in conjunction with a simple empirical ionization probability function. The IEA is a method used to describe multiple ionizations in fast ion-atom collision. Only one parameter p(b), the single electron ionization probability, is needed to calculate the multiple electron ionization cross section. A binomial distribution function is employed to calculate the probabilities for multiple electron removal. Previous applications of this method are described in references [42-44] and other references therein.

Since we are only interested in the cross sections for removing projectile electrons, we focus on the interactions between the projectile electrons and the target, as shown schematically in figure 16. It is assumed that the net probability of removing a single electron via the e-e and e-n interactions can be represented by an impact parameter dependent probability function $p(b)$. Then the differential cross section for removing a single electron may be expressed as

$$d\sigma = 2\pi\, p(b) b\, db \tag{4-4}$$

In the present experiments, the cross sections for the removal of specific numbers of electron have been measured. To calculate the probability of removing n and only n electrons from the total N electrons in the outermost shell of the projectile, we invoke

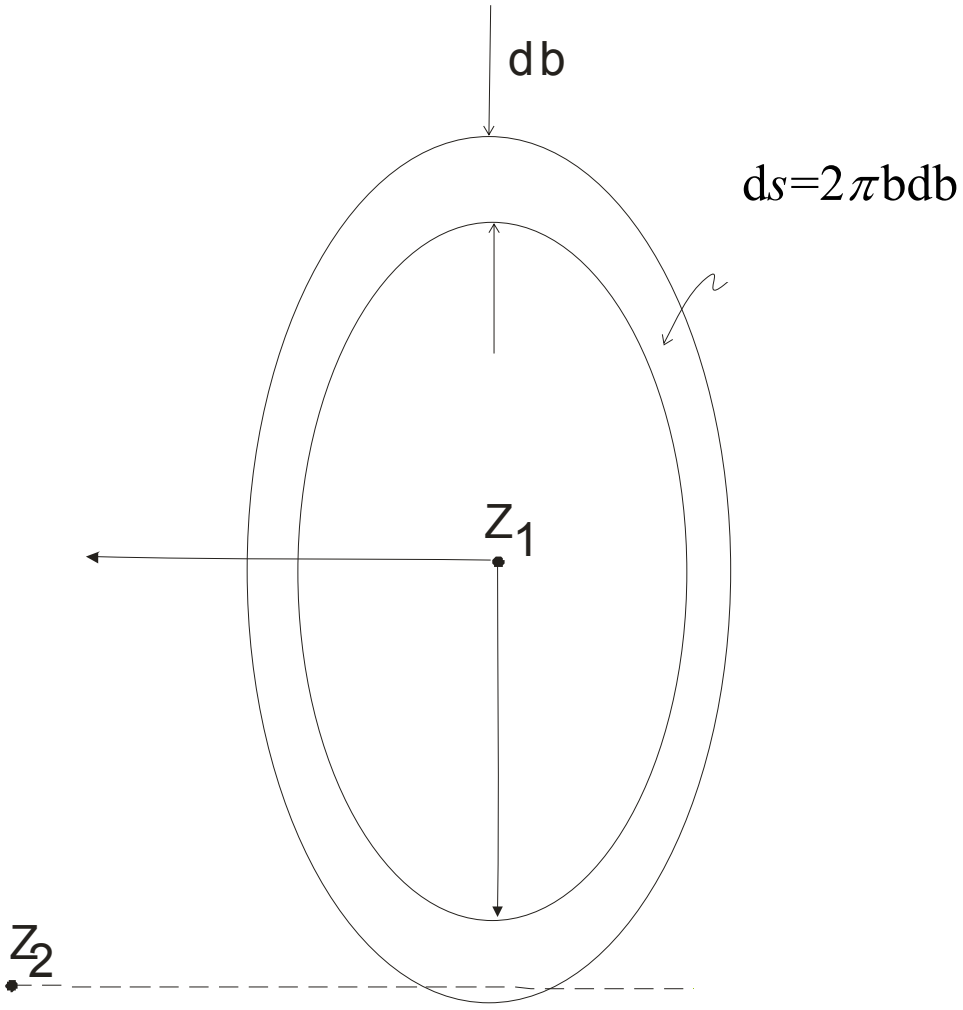

Figure 16. Schematic diagram showing the differential area associated with collisions having impact parameters between b and b+db.

the independent electron approximation which assumes that each of the n electrons is removed in a manner that does not affect the probability of removing any of the others.

This leads to a multiple-electron ionization probability that may be expressed in terms of a binomial distribution of the single electron ionization probabilities [40]. Specifically the probability of removing n electrons from an atomic shell containing N electrons is given by

$$P_n(b) = C_N^n \, p(b)^n [1 - p(b)]^{N-n} \tag{4-5}$$

where $C_N^n = \dfrac{N!}{n!(N-n)!}$

Then the cross section for removing n electrons may be computed from

$$\sigma_n = 2\pi \int_0^\infty P_n(b) \, b db \tag{4-6}$$

Two probability functions were used to simulate the probability of removing a single electron. One was the normal distribution function (Gaussian), $p(b) = p_0 e^{-b^2/2\delta^2}$, and the other was the exponential distribution function, $p(b) = p_0 e^{-b/r}$, where b represents the impact parameter relative to the target nucleus and p_0, r, and δ are probability, radius, and width fitting parameters, respectively. In the present application, only the eight outer-shell electrons were considered. Substitution of the Gaussian distribution function and equation (4-5) into equation (4-6), gives the following equation (4-7):

$$\sigma_n = 2\pi C_N^n \int_0^\infty (p_0 e^{-b^2/2\delta^2})^n (1 - p_0 e^{-b^2/2\delta^2})^{N-n} \, b db \tag{4-7}$$

Cross sections calculated using the above expression were fit to the experimental cross sections to determine the two unknown parameters p_0 and δ by means of a least squares precedure. Numerical integration was employed and all the calculations were processed using SigmaPlot® 2001. The best fits were obtained with the Gaussian function and are shown by the solid lines in figure 17. The fits improve as the target atomic number increases. The calculated cross sections and the two fitting parameters p_0 and δ are tabulated in Table III. The average absolute differences between the fitted and measured cross sections for n from 1 to 8 and the total are tabulated in Table IV.

The resulting values of the two fitting parameters (p_0 and δ) are plotted as functions of target atomic number in figure 18. The value of p_0 dramatically increases from He to Ne and remains nearly constant over the rest of the Z_2 range. The δ fitting parameter increases smoothly with the atomic number. These two parameters are accurately reproduced by the empirical formulas

$$p_0 = -0.16 + 1.16(1 - e^{-0.19Z_2}) \tag{4-8}$$

and

$$\delta = 0.060 + 0.16(1 - e^{-0.062Z_2}) \tag{4-9}$$

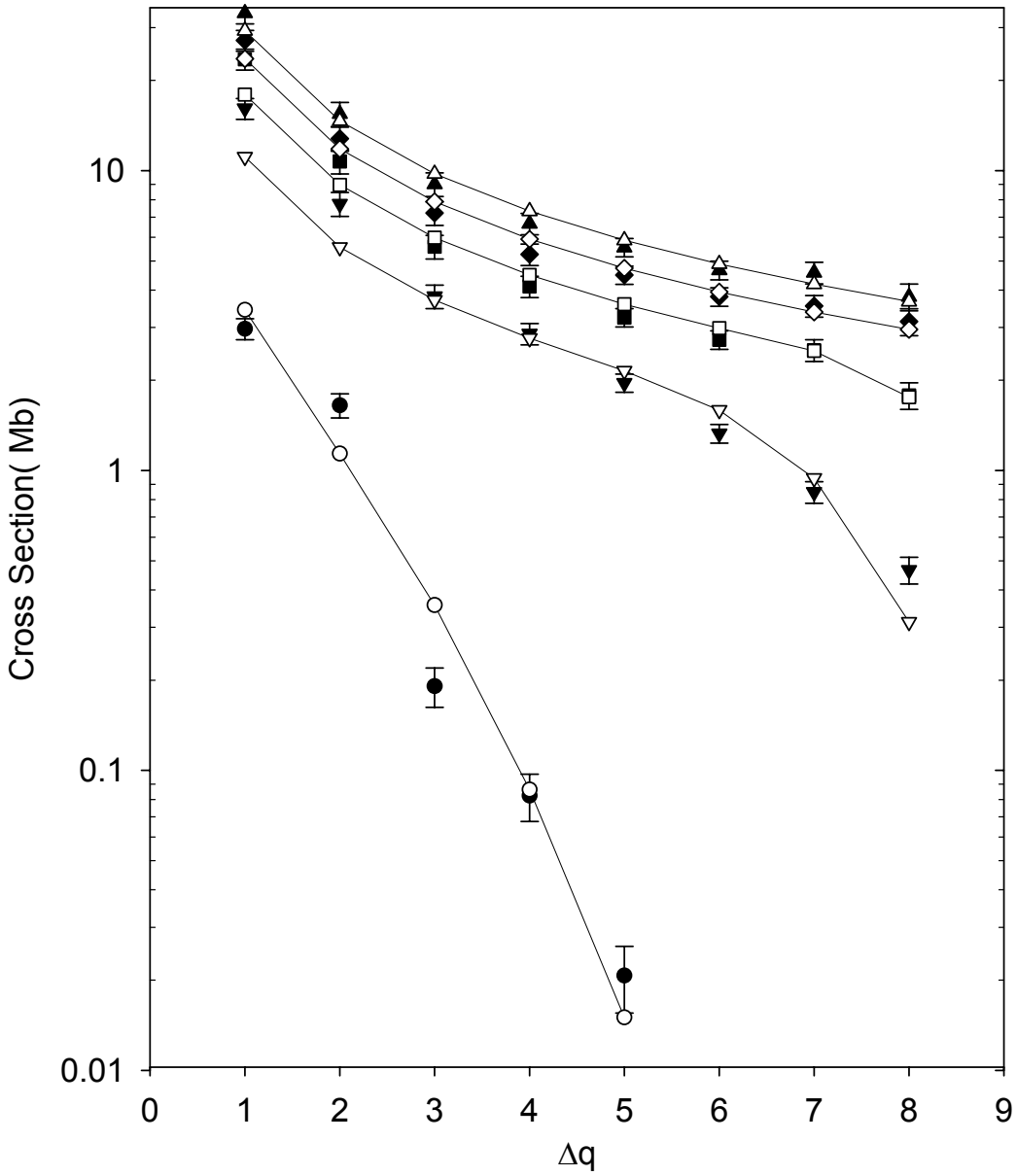

Figure 17. Electron loss cross sections plotted as a function of the number of electrons removed from the incident Xe^{18+} projectile (filled symbols). The solid lines and empty symbols show the results of fits to the data using the semiempirical IEA prescription described in the text.

Table III. Calculated cross sections obtained using a semiempirical procedure based on the IEA. The Gaussian distribution $p = p_0 e^{-\frac{b^2}{2\delta^2}}$ was used to represent the single electron loss probability.

Target		He	Ne	Ar	Kr	Xe
δ (Å)		0.077	0.13	0.17	0.19	0.22
p_0		0.21	0.83	0.97	1.00	1.00
Loss cross sections (Mb)	1	3.16	11.11	17.52	23.40	29.04
	2	0.98	5.56	8.76	11.70	14.52
	3	0.28	3.70	5.84	7.80	9.68
	4	0.061	2.76	4.38	5.85	7.26
	5	0.0096	2.15	3.50	4.68	5.81
	6		1.59	2.92	3.90	4.84
	7		0.94	2.45	3.34	4.15
	8		0.31	1.72	2.92	3.63
Total loss cross section(Mb)		4.49	28.14	47.09	63.61	78.94

Table IV. Comparison of the experimental electron loss cross sections with the cross sections obtained using the semiempirical fitting procedure in absolute percentage; $100\,|\frac{\sigma_{meas}-\sigma_{cal}}{\Delta\sigma_{meas}}|$. The last row lists the calculated $Z_{2(eff)}$ for the noble gases.

Δq	He	Ne	Ar	Kr	Xe
1	6.4	31.1	26.0	14.0	13.0
2	40.7	28.3	18.0	8.5	6.1
3	46.6	2.8	4.7	8.0	7.3
4	25.5	3.3	6.6	11.0	9.0
5	53.6	9.7	8.2	4.2	4.7
6		19.6	6.8	2.6	3.7
7		11.2	2.9	5.6	9.2
8		32.9	3.6	6.8	4.5
Average difference between the fit and the Measured loss cross section (%)	34.6	17.4	9.6	7.6	7.2

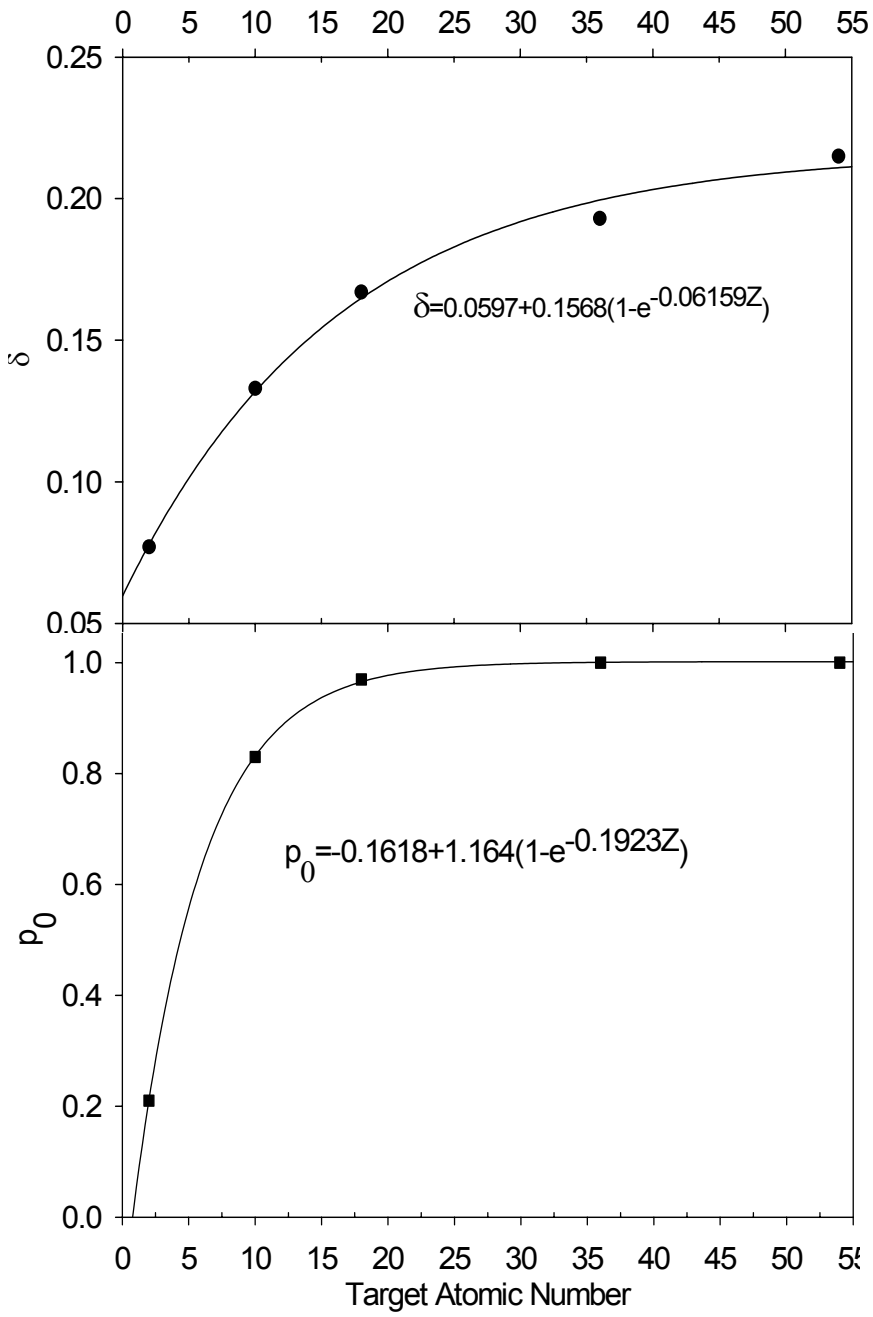

Figure 18. The fitting parameters p_0 and δ in the semiempirical IEA prescription described in the text plotted as functions of the target atomic number.

B. Molecular targets and cross section additivity

1. Cross sections for molecular gases

The measured electron capture cross section, the multiple electron loss cross sections and total electron loss cross sections for the molecular targets are tabulated in table V. The particular molecular targets used in this study were chosen to span as wide a range of average atomic number as possible within the constraints of being readily available and reasonably safe to handle. Unfortunately, no molecular gas targets having average atomic numbers beyond 18 fulfilled the latter condition. The gas targets used in this study have average atomic numbers between 1 (hydrogen) and 10 (SF_6). The target average atomic number, defined as $\overline{Z} = \sum_i f_i Z_i$, where f_i is the fraction of atoms in the molecule having atomic number Z_i, is tabulated in table V. By substitution of the average atomic number into equation (4-1), the predicated electron loss cross sections for molecular targets were calculated and the results are also listed in table V.

Table V. Electron capture and loss cross sections for 6 MeV/amu Xe^{18+} in molecular targets as a function of Δq, the change in projectile charge. All cross sections are in units of Mb/atom. The predicted loss cross sections are calculated by using equation 4-1

	H_2	CH_4	C_3H_8	SiH_4
Average atomic #	1.00	2.00	2.36	3.60
Δq	Cross Section	Cross Section	Cross Section	Cross Section
-1	0.0021 ±0.00	0.05 ±0.01	0.05 ±0.01	0.041 ±0.009
1	1.2 ±0.11	3.1 ±0.3	3.4 ±0.3	5.1 ±0.5
2	0.6 ±0.06	1.7 ±0.2	2.0 ±0.2	2.2 ±0.2
3	0.067 ±0.00	0.44 ±0.04	0.59 ±0.06	1.1 ±0.1
4	0.038 ±0.00	0.28 ±0.03	0.34 ±0.03	0.86 ±0.08
5	0.02 ±0.00	0.12 ±0.01	0.17 ±0.02	0.60 ±0.06
6	0.007 ±0.00	0.06 ±0.01	0.084 ±0.008	0.50 ±0.05
7		0.028 ±0.003	0.044 ±0.005	0.39 ±0.04
8		0.012 ±0.002	0.009 ±0.001	0.23 ±0.03
>9				0.33 ±0.05
Total loss cross section	1.9 ±0.2	5.8 ±0.3	6.5 ±0.4	11.3 ±0.5
Predicted Total loss cross section	1.50	5.2	6.5	11.1
Absolute difference %	21.0	10.3	0.0	1.8

Table V (Continued)

		N_2	CO	CO_2
Δq	Average atomic #	7.00	7.00	7.33
		Cross Section	Cross Section	Cross Section
-1		0.41 ±0.09	0.21 ±0.05	0.27 ±0.06
1		11 ±1	11 ±1	13 ±1
2		6.80 ±0.6	6.3 ±0.6	6.8 ±0.7
3		2.9 ±0.3	2.5 ±0.2	2.8 ±0.3
4		1.8 ±0.2	1.6 ±0.2	1.7 ±0.2
5		1.0 ±0.1	0.88 ±0.08	0.99 ±0.09
6		0.55 ±0.06	0.53 ±0.05	0.54 ±0.05
7		0.28 ±0.03	0.30 ±0.03	0.31 ±0.03
8		0.11 ±0.01	0.12 ±0.02	0.11 ±0.02
>9			0.053 ±0.008	0.032 ±0.005
Total loss cross section		25 ±1	24 ±1	26 ±1
Predicted Total loss cross section		23.6	23.6	24.8
Absolute difference percentage		5.6	1.7	4.6

Table V (Continued)

		O_2	C_3F_8	CF_4	SF_6
Δq	Average atomic #	8.00	8.18	8.40	10.00
		Cross Section	Cross Section	Cross Section	Cross Section
-1		0.22 ±0.05	0.21 ±0.05	0.26 ±0.06	0.21 ±0.05
1		13 ±1	12 ±1	12 ±1	15 ±1
2		7.1 ±0.7	7.4 ±0.7	6.5 ±0.6	7.9 ±0.8
3		3.2 ±0.3	3.7 ±0.3	3.3 ±0.3	4.2 ±0.4
4		2.1 ±0.2	2.5 ±0.2	2.3 ±0.2	2.9 ±0.3
5		1.3 ±0.1	1.6 ±0.2	1.4 ±0.1	2.0 ±0.2
6		0.77 ±0.08	1.1 ±0.1	1.0 ±0.1	1.4 ±0.1
7		0.47 ±0.05	0.68 ±0.07	0.60 ±0.07	1.0 ±0.1
8		0.19 ±0.03	0.34 ±0.04	0.27 ±0.04	0.59 ±0.08
>9			0.26 ±0.04	0.09 ±0.01	0.60 ±0.09
Total loss cross section		28 ±1	30 ±1	28 ±1	36 ±2
Predicted Total loss cross section		27.3	28.0	28.8	34.7
Absolute difference percentage		2.5	6.7	2.8	3.6

2. The dependence of total loss cross sections on target average atomic number

The total electron loss cross sections per atom obtained in this study are shown in figure 19, plotted as a function of the target average atomic number. The per atom cross section is the cross section per molecule divided by the number of atoms per molecule. The dashed line in Figure 19 is the same line defined by the total electron loss cross sections for the monatomic targets He and Ne in Figure13. It is evident from the figure that the per atom total electron loss cross sections for the molecular targets (i) increase linearly with target average atomic number, and (ii) closely correspond to the predicted cross sections for atomic targets having $Z = \overline{Z}$. This observation means that the following additivity rule applies to the molecular data:

$$\sigma_{per\_mol} = N\sigma(\overline{Z}) \tag{4-10}$$

where σ_{per_mol} is the cross section per molecule, N is the number of atoms per molecule, and $\sigma(\overline{Z})$ is the cross section for an atom having an atomic number equal to the average atomic number of the molecule. By substitution of the corresponding average atomic number ($\overline{Z}$) of each molecular target into equation (4-1), the predicted cross sections can be calculated and they also are listed in table V. The absolute percentage differences between the experimental cross sections and the predicted cross sections are listed in table V. All the differences are within ±6.7%, except for the two lightest targets hydrogen and methane, which deviate by 21.0% and 10.3%, respectively. All the predicted cross sections are lower than the experimental cross sections except for CF_4 which is slightly higher (2.8%) than the experimental cross section.

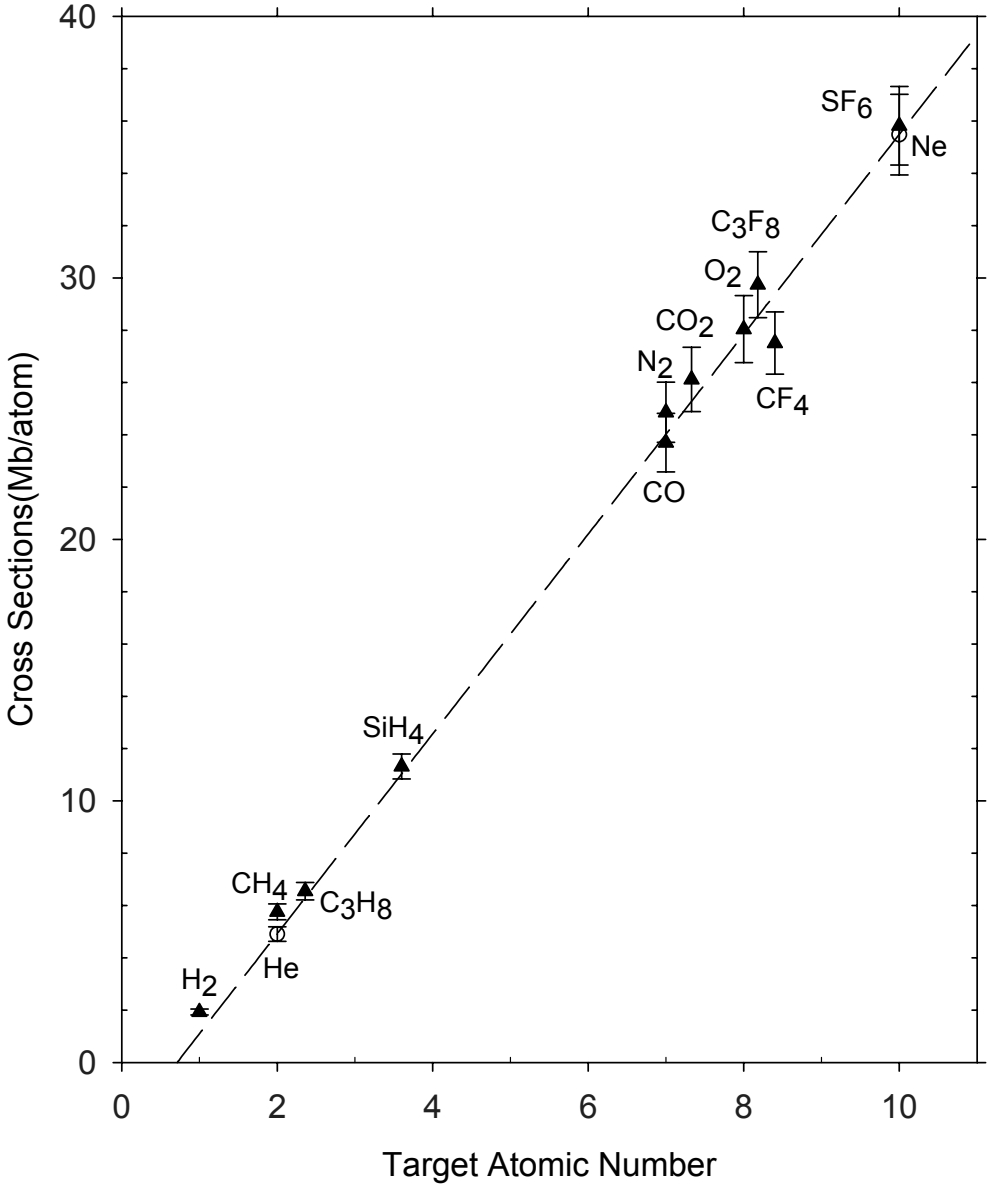

Figure 19. Total loss cross section (per atom) for 6 MeV/amu Xe^{18+} projectile in various molecular targets plotted as a function of target average atomic number. The dashed line is the same line that was defined by the He and Ne data points (shown here by empty circles) in figure 13.

3. Additivity rule

The usual form of the additivity rule is

$$\sigma_{mol} = \sum_i n_i \sigma(Z_i) \tag{4-11}$$

where n_i is the number of atoms in the molecule with atomic number Z_i. The validity of this rule was tested by using the linear relationship between the total loss cross section and the target atomic number, as defined by the noble gas data, to calculate the $\sigma(Z_i)$. For example, the measured total electron loss cross section per atom for CO is 24±1 Mb/atom, while the cross section calculated by using equation (4-1) and (4-11) is 23.6 Mb/atom. An example for CF_4 is by substitution of the cross section for carbon (19.9 Mb) and fluorine (31.0 Mb) into equation (4-11) to get the total cross section 143.9 Mb while the measured total loss cross section is (28±1 Mb/atom)×5 = 140±5 Mb. The results for other molecular targets are shown in Figure 20, where the ratio of the measured cross section to the cross section calculated using the additivity rule (equation 4-11) is plotted versus the average atomic number. As shown in table V and figure 20, the additivity rule yields total electron loss cross sections that differ from experimental data by less than 6.7%, except for the H_2 (not shown in figure 20) and CH_4 targets. The large ratio exhibited by H_2 may indicate that the dependence on Z_2 for atomic targets becomes nonlinear below He. However, similar large deviations from the additivity rule have been observed in cross sections for single electron capture by heavy ions from H_2 targets. An analysis based on the Bohr-Lindhard model presented by Knudsen *et al.* [35] predicts a limiting value of the single electron capture cross section

ratio $\sigma(H_2)/\sigma(H)$ of 3.8 for $E/q^{4/7}>10^2$, where E is the projectile energy in units of KeV/amu and q is the projectile charge. Rather coincidentally, the ratio of the present total electron loss cross sections obtained using equation (4-1) to calculate $\sigma(H)$ is 3.4.

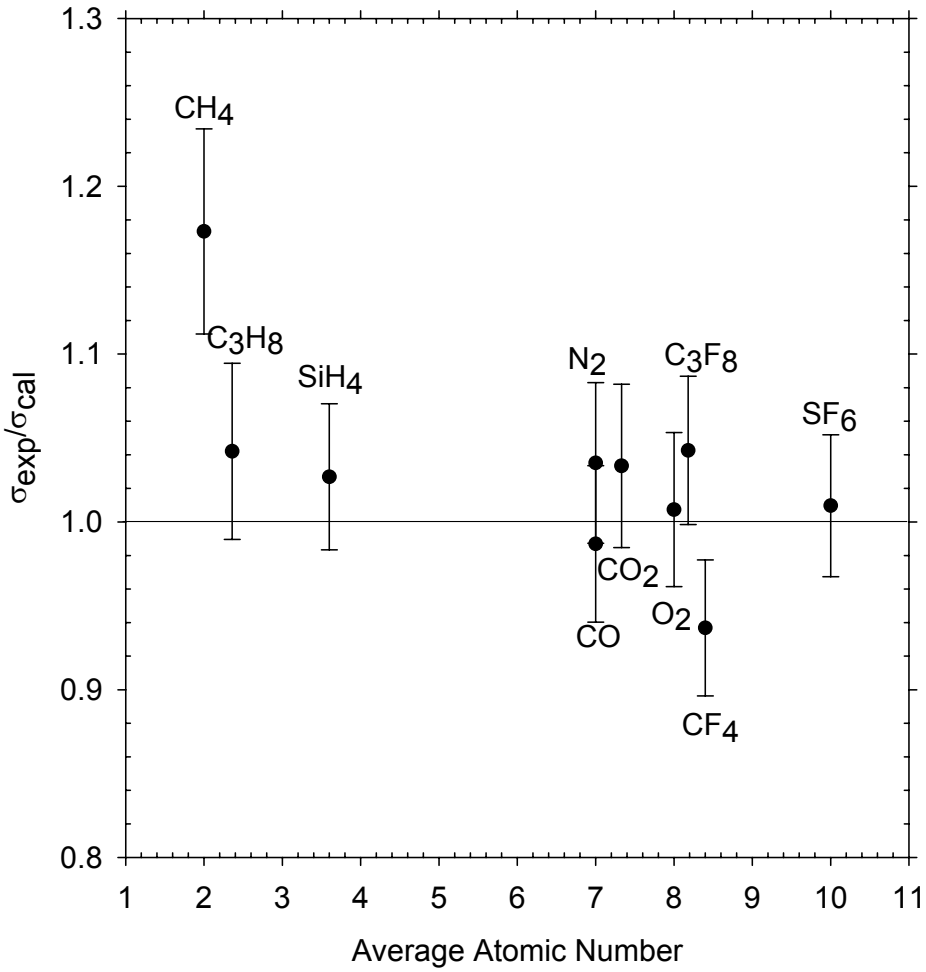

Figure 20. Ratio of the measured total electron loss cross section and the cross section calculated using the additivity rule expressed by equation (4-11), plotted versus the target average atomic number.

4. The effect of molecular structure on the electron loss cross sections

In figures 21 and 22, the $\sigma(\Delta q)$ are compared for different molecular targets having nearly the same average atomic number. These figures show that the electron loss cross sections for specific Δq are remarkably similar for targets within the same $\overline{Z}$ group. However, a slight dependence of the cross sections on the number of atoms per molecule may be indicated by the data in figure 22, especially at the higher values of Δq. It is reasonable to expect such a behavior because, as the number of atoms in a molecule increases, it becomes more likely that the projectile will experience collisions with several atoms while traversing through the molecule. A comparison of the cross sections for the atomic target Ne and the molecular target SF_6 is shown in figure 23. It appears that the cross sections for high $\Delta q \geq 5$ are somewhat larger in the molecular target, but the effect is surprisingly weak.

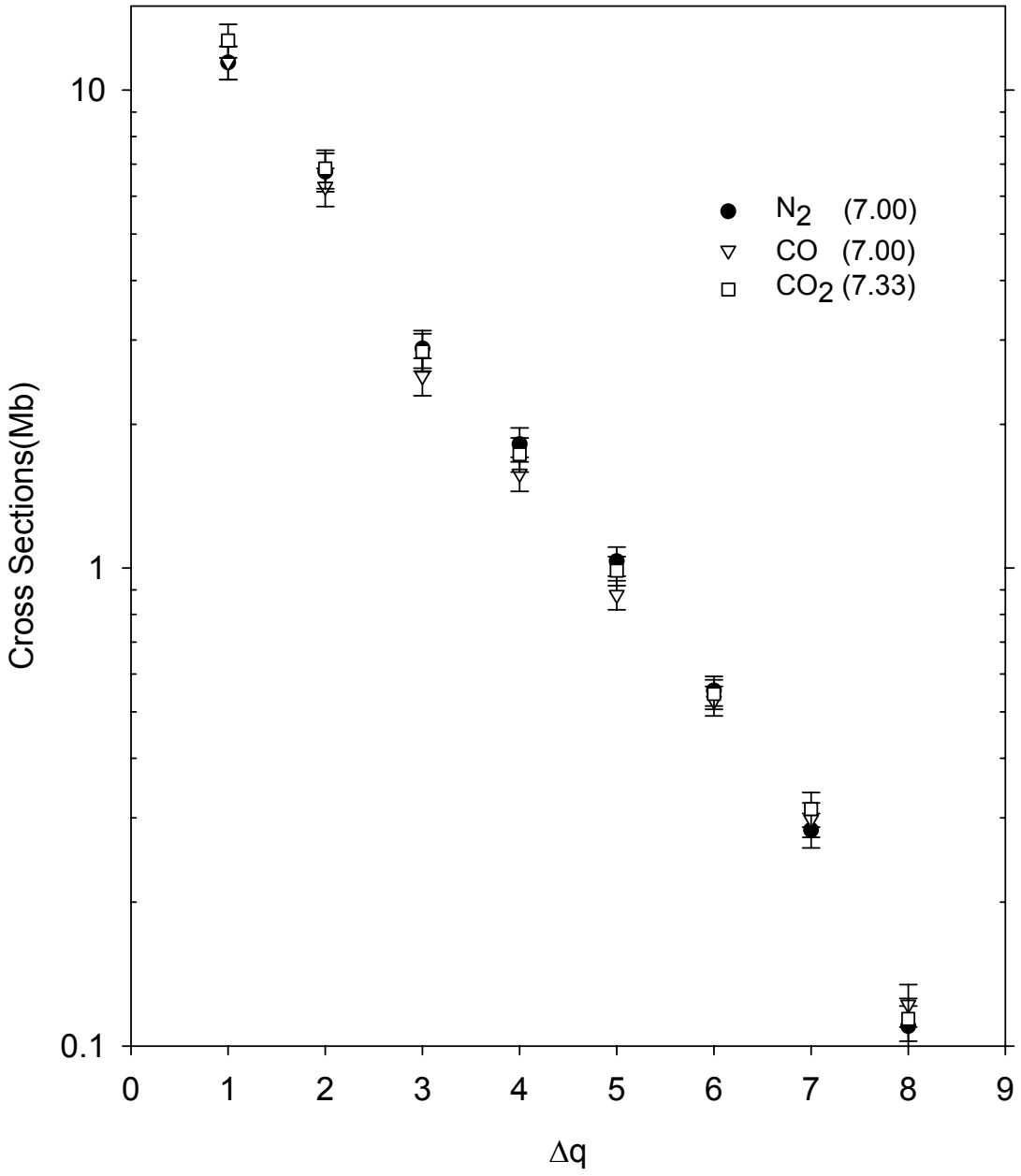

Figure 21. Comparison of cross sections for the loss of one to eight electrons in the molecular targets N_2, CO, and CO_2. Average atomic numbers are indicated in parentheses.

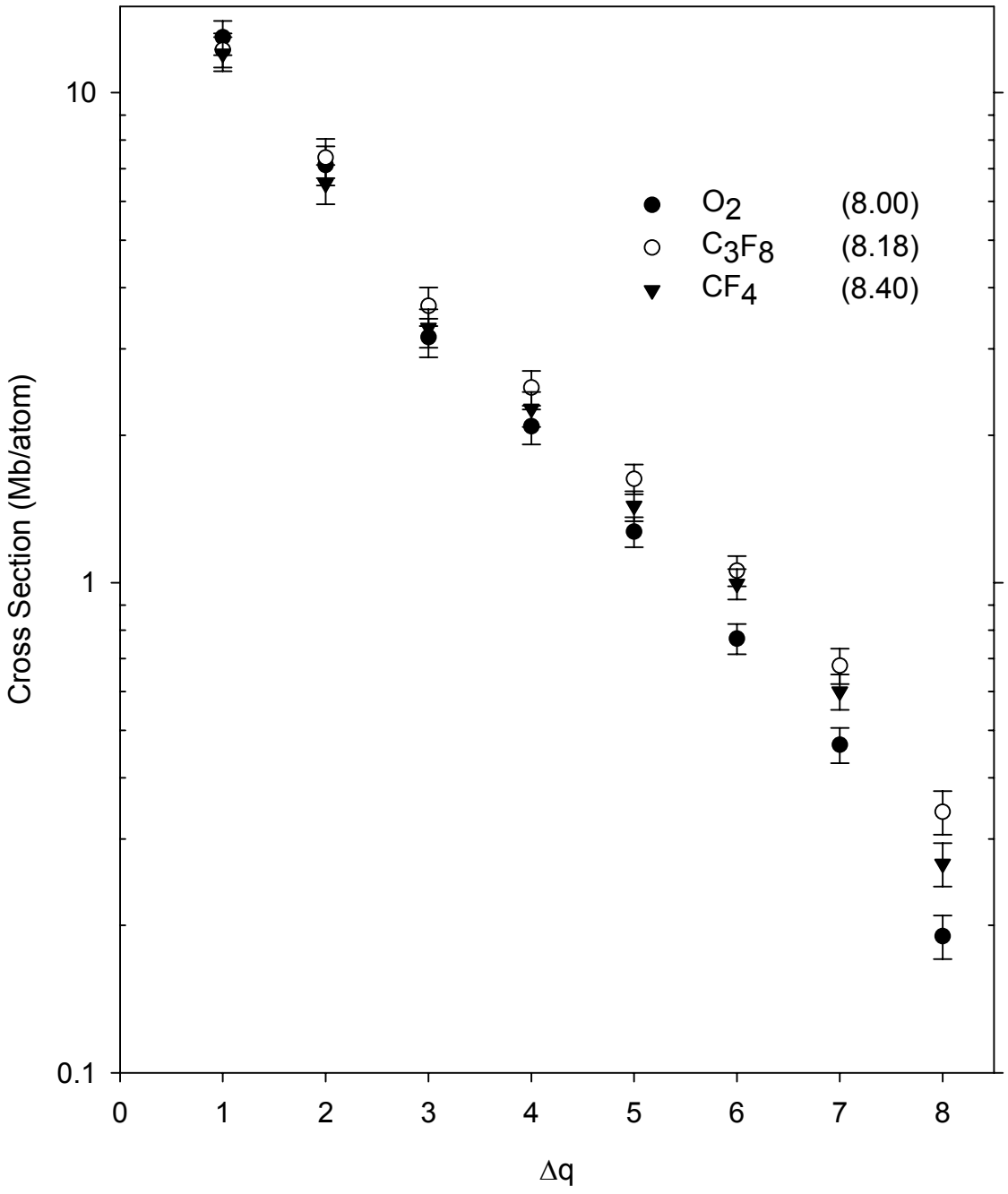

Figure 22. Comparison of cross sections for the loss of one to eight electrons in the molecular targets O_2, C_3F_8, and CF_4. Average atomic numbers are indicated in parentheses.

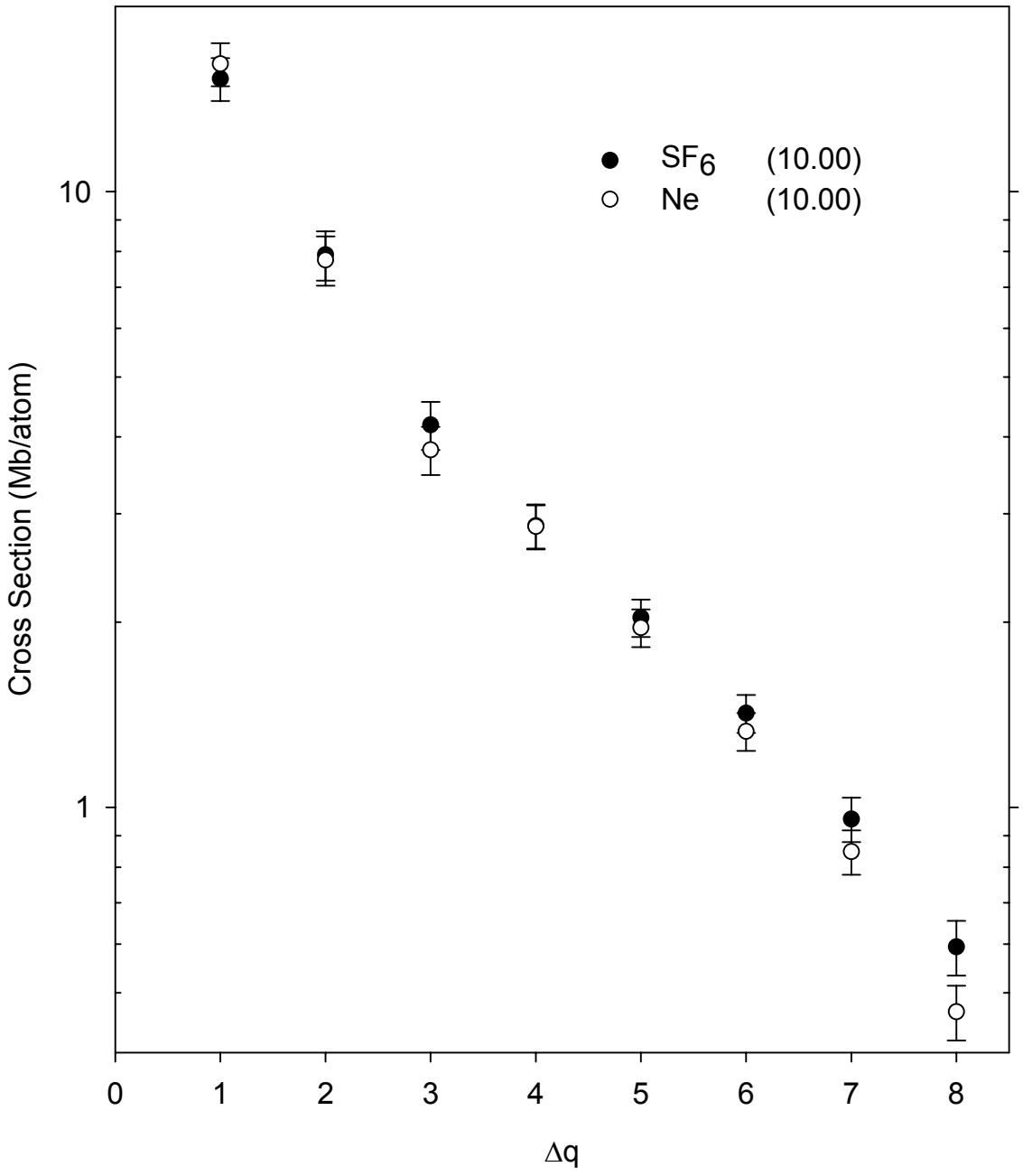

Figure 23. Comparison of cross sections for the loss of one to eight electrons in the molecular target SF6, and atomic target Ne. Average atomic numbers are indicated in parentheses.

One possible explanation for the insensitivity of the electron loss cross sections to molecular structure is that the average impact parameter for electron loss is much smaller than the target molecular bond length. This conjecture may be tested by calculating the most probable impact parameter $b_n^{'}$ associated with collisions in which the projectile loses n electrons. The calculation procedure is described as follows. Using equation (4-8) and (4-9), the value of p_0 and δ were calculated for the atoms in the molecular targets (these results are listed in table VI). Then the distribution function $\sigma_n^{'}$, defined as

$$\sigma_n^{'} = 2\pi b P_n(b) \tag{4-12}$$

where $P_n(b) = C_N^n (p_0 e^{-b^2/2\delta^2})^n (1 - p_0 e^{-b^2/2\delta^2})^{N-n}$,

was calculated as a function of b.

Figure 24 shows the calculated $\sigma_n^{'}$ as a function of impact parameter b for collisions with a sulfur atom target. Finally $b_n^{'}$ was determined by finding the value of the impact parameter corresponding to the maximum value of $\sigma_n^{'}$. Using this same procedure, the $b_n^{'}$ for the other molecular target atoms were calculated and the results are tabulated in table VII for n=1 to 8.

In figure 25, $b_n^{'}$ is plotted as a function of the target atomic number for n=1 to 8. From this figure it is clear that $b_n^{'}$ increases faster in the region of light atoms than in the region of heavy atoms (Z_2>18). Furthermore, $b_n^{'}$ is plotted as a function of Δq in figure

26 for the noble gas targets and hydrogen. It shows that $b_n^{'}$ decreases sharply from $b_1^{'}$ to $b_2^{'}$ which is consistent with the decrease for the multiple electron loss cross section from 1 loss to 2 loss.

Another important parameter is the radius of Xe^{18+}, which was calculated using a Dirac-Fock program [45]. Its value was found to be 0.32 Å. Other parameters, such as target atomic radii and molecular bond lengths, are listed in tables VI and VIII, repectively.

A schematic illustration is given in figure 27 for SF_6 in which the most probable impact parameters for one-electron loss in collisions with F and S atoms are compared to the S-F bond length. It is assumed that the target is stationary and only the projectile is moving. Only four out of six fluorine atoms are shown in the figure. The solid circles represent the average radii of the outermost shells of the atoms. The dotted circles represent the most probable impact parameters for

Table VI. Radii of the target atoms [46, 47], and calculated p_0 and δ parameters

atom	p_0	δ (Å)	Radius(Å)
H	0.041831	0.069066	0.53
C	0.635033	0.108143	0.67
N	0.699265	0.114615	0.56
O	0.752261	0.120701	0.48
F	0.795985	0.126423	0.42
Si	0.92336	0.150298	1.11
S	0.948532	0.15797	0.88

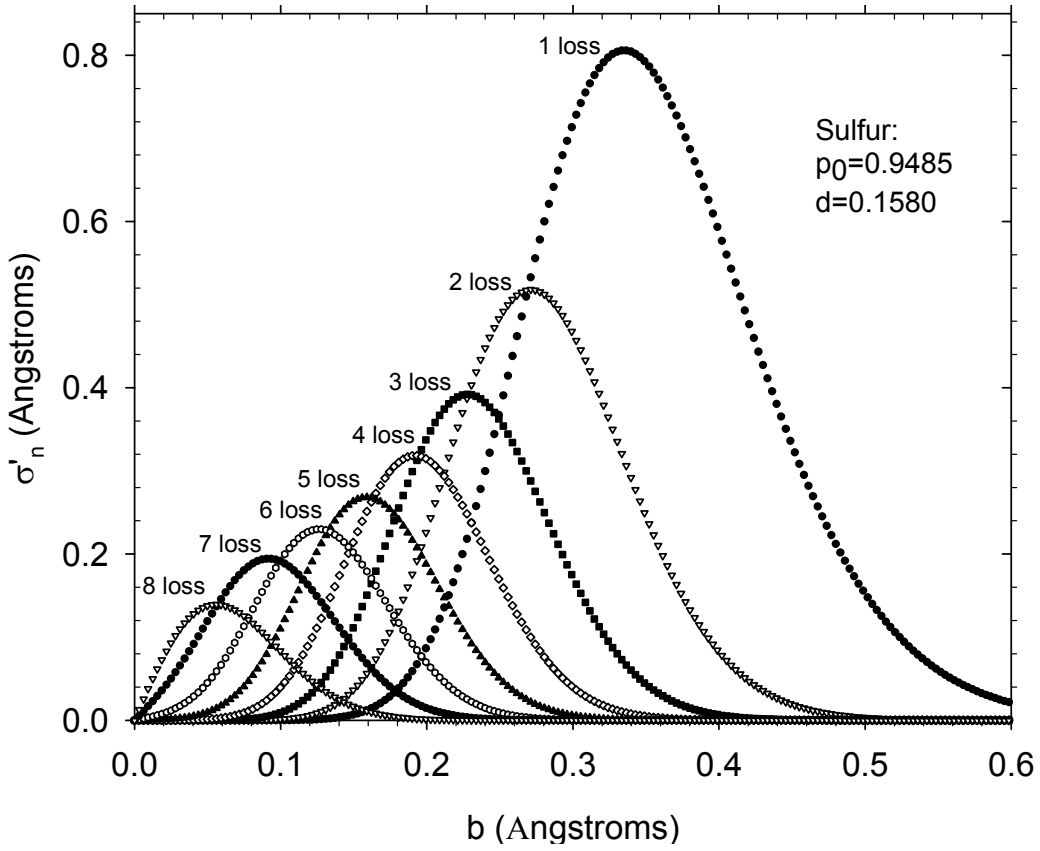

Figure 24. Calculated $\sigma_n^{'}$ vs. impact parameter b for one to eight electron loss in collision with sulfur atoms.

Table VII. The most probable impact parameters for electron loss from 6 MeV/amu Xe^{18+} ion in collisions with atomic targets (in Å)

Atom / Δq	H(1)	He(2)	Li(3)	C(6)	N(7)	O(8)	F(9)	Ne(10)	Si(14)	S(16)	Kr(36)	Xe(54)
1	0.0748	0.1153	0.1465	0.2119	0.2275	0.2431	0.2587	0.2712	0.3179	0.3366	0.427	0.4519
2	0.053	0.0748	0.0997	0.1621	0.1777	0.1932	0.2057	0.2182	0.2556	0.2712	0.3491	0.3678
3	0.0405	0.0561	0.0717	0.1278	0.1434	0.1558	0.1683	0.1808	0.2151	0.2275	0.293	0.3117
4	0.0343	0.0436	0.0561	0.0997	0.1122	0.1247	0.1371	0.1465	0.1808	0.1932	0.2493	0.2649
5	0.0312	0.0374	0.0436	0.0748	0.0873	0.0997	0.1091	0.1184	0.1465	0.159	0.2088	0.2213
6	0.0281	0.0343	0.0374	0.0561	0.0655	0.0748	0.081	0.0904	0.1153	0.1278	0.1683	0.1808
7	0.0249	0.0312	0.0343	0.0468	0.0499	0.0561	0.0592	0.0655	0.0842	0.0904	0.1278	0.134
8	0.0249	0.0281	0.0312	0.0374	0.0405	0.0436	0.0436	0.0468	0.053	0.0561	0.0717	0.0748

Table VIII. Molecular bond lengths [45, 46]

Bond	$H-H$	$C-H$	$C-C$	$Si-H$	$C-F$	$C-O$	$C=O$	$S-F$	$N\equiv N$	$O=O$
Bond length (Å)	0.75	1.08	1.1	1.48	1.35	1.43	1.2	1.56	1.1	1.21

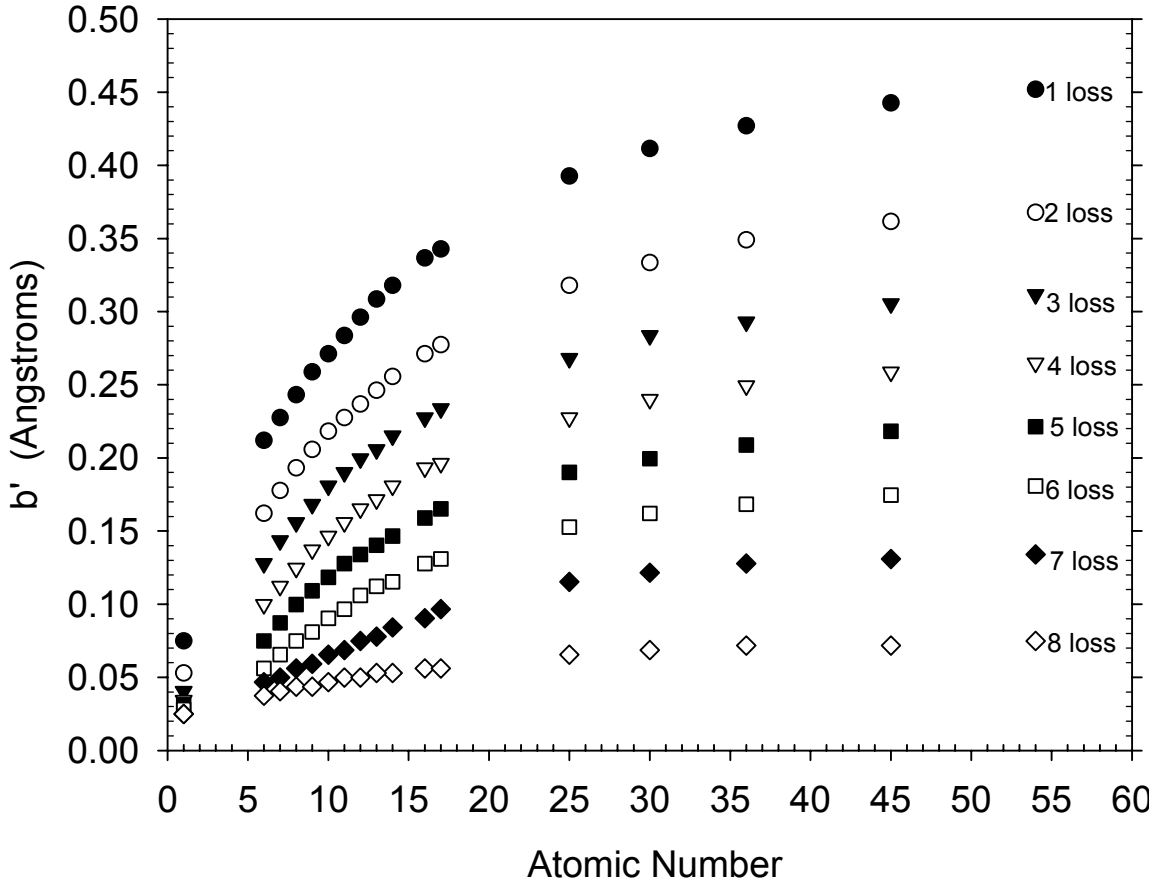

Figure 25. The most probable impact parameters for one to eight electron loss are plotted as a function of the target atomic number.

one-electron loss while the long dashed circles represent the outer shell radius of the projectile when it is centered on the dotted circles. From table VI, table VII, table VIII and the calculations, the radii of S, F and Xe^{18+} are 0.88, 0.42 and 0.32 Å, respectively; the bond length of S-F is 1.56 Å; $(b_1')_S$ and $(b_1')_F$ are 0.34 Å and 0.26 Å, respectively.

Since the sum of the most probable impact parameters for electron loss collisions with S and F (0.60 Å) is much less than the S-F bond length (1.56 Å), it is unlikely that the projectile will undergo an electron loss collision with more than one atom in the molecule. Therefore, it may be concluded, that it is the small impact parameters which are responsible for the insensitivity of the electron loss cross sections to the molecular structure.

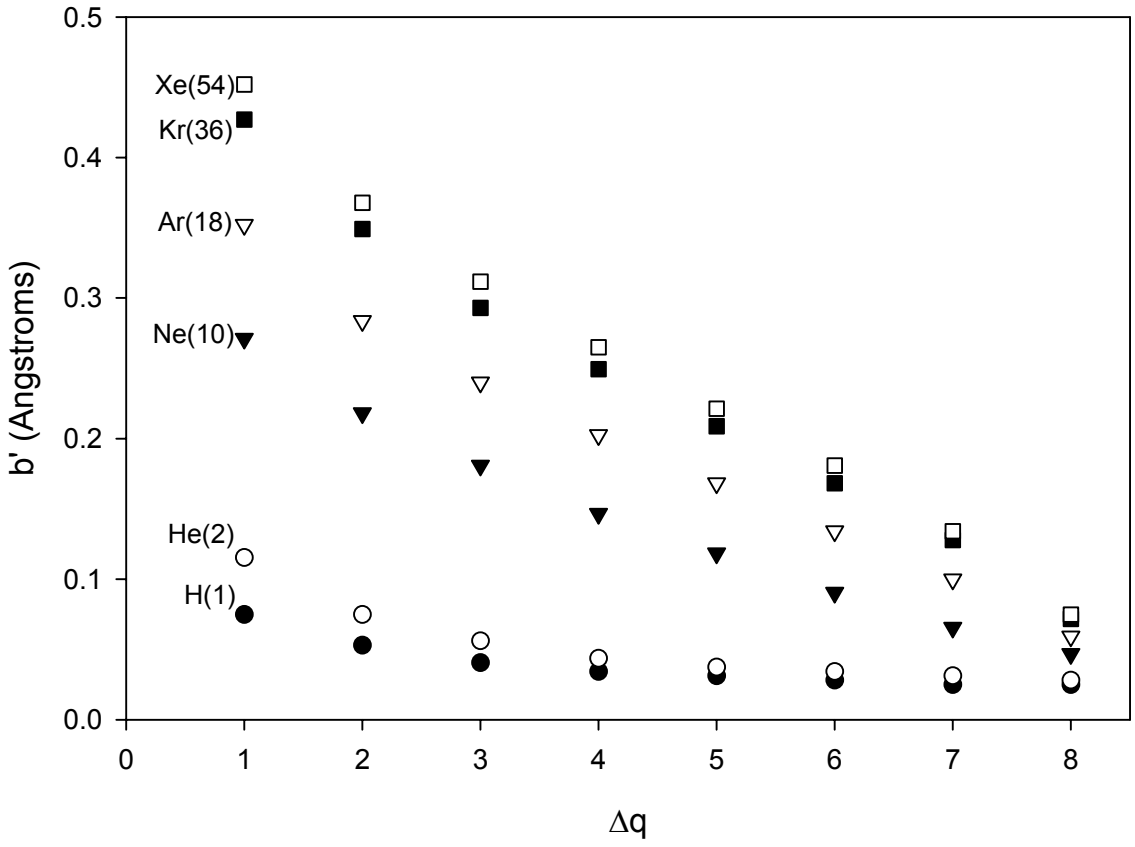

Figure 26. The most probable impact parameter plotted as a function of Δq.

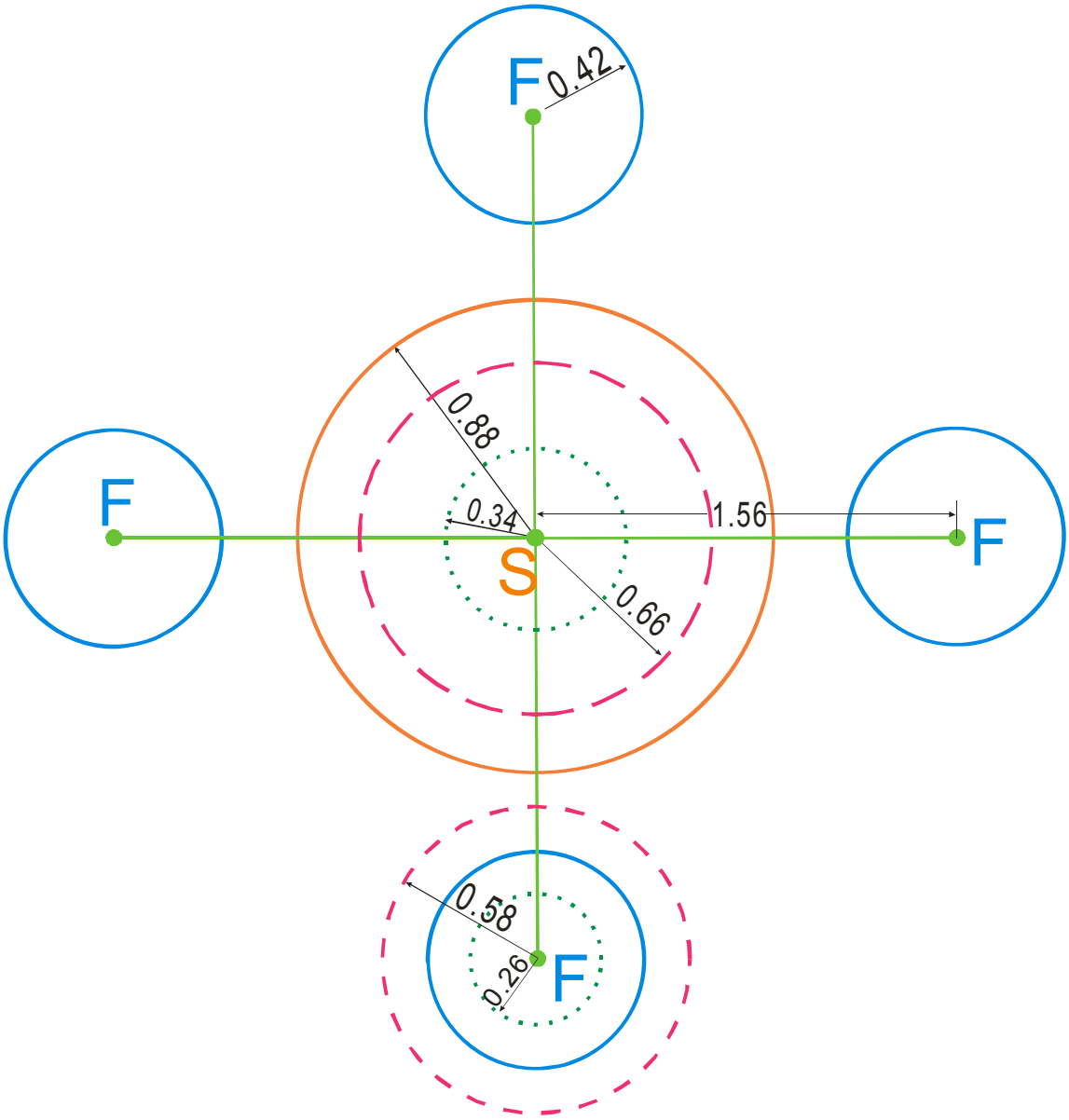

Figure 27. Schematic diagram comparing the most probable impact parameters for one-electron loss collisions of 6 MeV/amu Xe^{18+} with S and F atoms to the S-F bond length in SF_6. The radii are defined in the text. All the units are in Angstroms.

5. Average electron loss per collision

The average electron loss from a projectile having incident charge q in a single collision with a target atom (or molecule) can be calculated by means of the following expression

$$\Delta\bar{q} = \frac{\sum_{\Delta q} \Delta q \sigma_{q,q+\Delta q}}{\sigma_T} \tag{4-13}$$

in which σ_T is the total electron loss cross section. The calculated average electron loss per collision $\Delta\bar{q}$ for all the targets is plotted as a function of the target (average) atomic number in figure 28. Open circles represent the noble gas targets and are well reproduced by the function

$$\Delta\bar{q} = a(1 - e^{-1/bZ_2}) + c(1 - e^{-dZ_2}) \quad , \tag{4-14}$$

shown by the solid curve in the figure. The best fit parameter values are a=1.216, b=0.03858, c=2.018, and d=0.08287. The $\Delta\bar{q}$ for molecular targets were calculated using the same method and the results are shown as solid circles in figure 28. It is evident that the $\Delta\bar{q}$ for the molecular targets cluster about the solid curve defined by the noble gas values except in the case of SiH_4, which is far above the curve. The reason for the large deviation exhibited by SiF_4 is presently unknown.

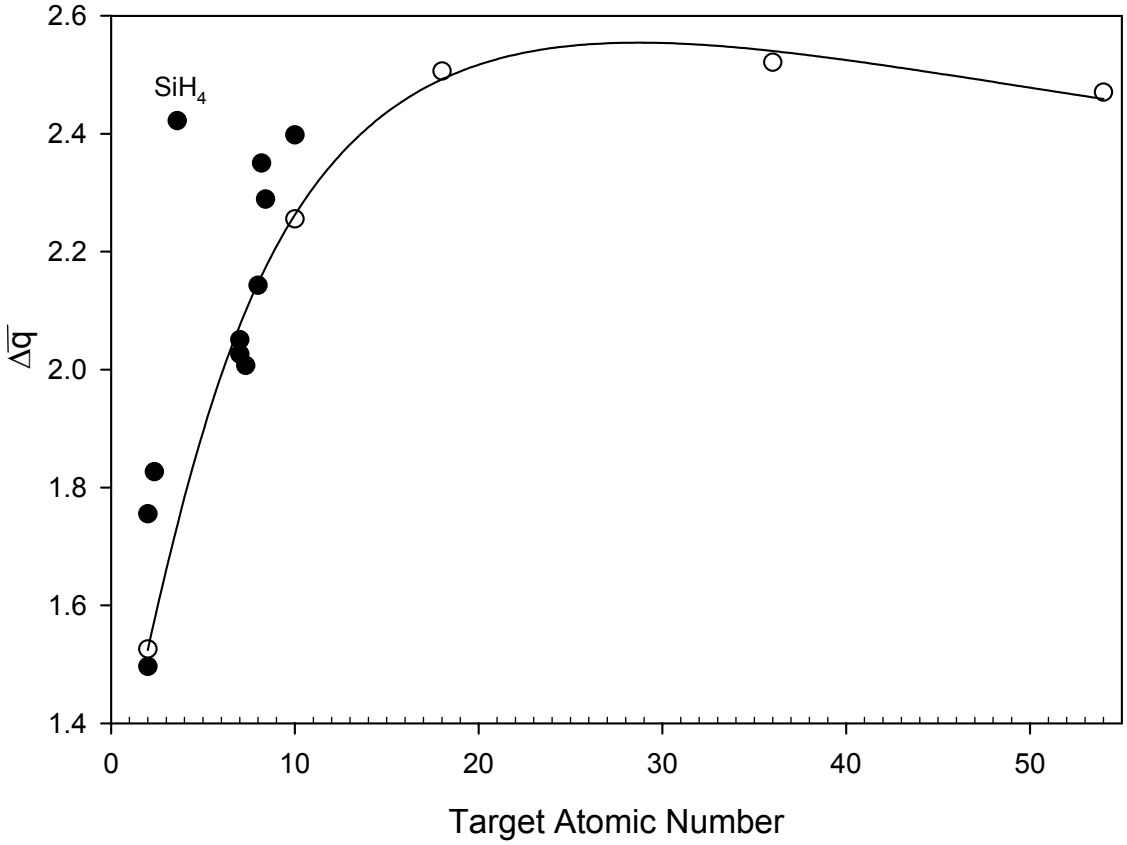

Figure 28. The average number of electrons lost from 6 MeV/amu Xe^{18+} ions in single collisions as a function of target (average) atomic number. The open circles represent the noble gas targets while solid circles represent the molecular targets. The solid line is fit to the noble gas data.

CHAPTER V

CONCLUSIONS

Cross sections for the loss of one through eight electrons from 6 MeV/amu Xe^{18+} in single collisions with noble gas and molecular gas targets have been measured. The results for noble gases show that: a) the one electron loss cross section is much larger than the cross section for multiple loss; b) the multiple loss cross sections of the projectile decrease exponentially with increasing number of electrons removed but, at the higher values of Δq, the rate of decrease is much slower than that at low values of Δq for $Z_2 \geq 10$; c) the dependence of the electron loss cross sections on the number of electrons removed is well represented by a single exponential function in the case of a He target, while two exponential functions are required to describe the Δq dependence of the other noble gas targets; and d) the average electron loss per collision increased steeply from He to Ar and then became almost constant from Ar to Xe.

The observed dependence of the total loss cross section on target atomic number for noble gas targets is defined by two straight line segments; one extending from He to Ne with a relatively steep slope and the other extending from Ar to Xe with a much smaller slope. The predictions of n-body CTMC calculations are in good agreement with the total electron loss cross sections and reproduce the main features of the observed Z_2-dependence.

In an effort to develop a scaling procedure for predicting the individual electron loss cross sections for any Z_2, a semiempirical method based on the IEA was employed. It provided a reasonably good representation of the cross sections for all of the noble gas targets except for He.

The single electron capture cross section was also measured for the noble gas targets. It was found that He has the smallest capture cross section while Ne has the largest. Following the abrupt increase from He to Ne, the capture cross section slowly decreased from Ne to Xe.

The electron loss cross sections were measured for a variety of molecular targets. The total electron loss cross section divided by the number of atoms per molecule plotted versus target average atomic number, closely mirrored the straight line Z_2-dependence established by the cross sections for the atomic targets He and Ne. An additivity rule stating that the total electron loss cross section for a molecular target is equal to the sum of the total electron loss cross section of its atomic constituents was tested by using the straight–line Z_2 dependence established by the measurements for He and Ne to calculate the constituent cross section. The ratios of the predicated total electron loss cross section to the experimental total electron loss cross section were found to deviate from unity by an absolute average of 6.7% except for H_2 and CH_4. Therefore, it was concluded that cross section additivity works well for electron loss from heavy ions in the present energy and charge regime. This implies that the target molecules act as assemblies of individual atoms and alterations of electron densities and ionization energies due to molecular bonding do not significantly

influence the electron loss cross sections. Further confirmation of this hypothesis was provided by comparisons of the individual cross sections as a function of Δq, which showed only a slight dependence on the molecular nature of the target at the higher values of Δq. A comparison of the most probable impact parameters for electron loss collision with molecular bong lengths provided a plausible explanation for the insensitivity of the cross sections to the molecular nature of the target. In the case of SF_6, for example, it was estimated that the most probable impact parameters for single electron loss collisions with F atoms and S atoms are 0.26 Å and 0.34 Å, respectively, while the S-F bond length is 1.56 Å. Therefore, it may be concluded that an electron loss collision with more than one atom in the SF_6 molecule is very unlikely.

REFERENCES

1. R. A Gough, and M. L. Mallory, IEEE Trans. Nucl. Sci. **NS-26**(2), 2384(1979).
2. H. H. Bransden and M. R. C. McDowell, *Charge Exchange and the Theory of Ion-Atom Collisions* (Clarendon Press, Oxford, 1992).
3. G. Steigman, Astrophys. J. **199**,642(1975).
4. T. F. Godlove, IEEE Trans. Nucl. Sci. **NS-26**(3) 2997(1979).
5. E. Nardi and Z. Zinamon, Phys. Rev. Lett., **49**, 1251(1982).
6. R. K. Janev, *Atomic and Molecular Processes in Fusion Edge Plasmas* (Plenum, New York, 1995).
7. J. D. Lindl, *Inertial Confinement Fusion* (Springer, New York, 1998).
8. J. D. Lindl, R. L. McCrory, and E. M. Campbell, Phys. Today **45**(9), 32 (1992).
9. R. M. White, D. A. Resler, and S. I. Warshaw, "Evaluation of charged-particle reactions for fusion applications," *Proceedings of the International Convergence on Nuclear Dtata for Science and Technology 1991*, Julich, Germany, Edited by S. M. Qaim (Springer-Verlag, Berlin, 1992), p.183.
10. R. O. Bangerter, Fusion Engineering and Design **32-33**, Issues 1-4, (November 1996), p. 27-32; D. A. Callahan, Fusion Engineering and Design **32-33**, Issues 1-4, (November 1996), p. 441-452.
11. D. Mueller, L Grisham , I. Kaganovich, R. L. Watson, V. Horvat, K. E. Zaharakis and M. S. Armel, Physics of Plasmas, **8**(5), 1753(2001).
12. V. S. Nikolaev, Sov. Phys. Usp. **8**, 269 (1965).

13. Hans-Dieter Betz, Rev. Mod. Phys. **44**, 465 (1972).

14. H. Tawara and A. Russek, Rev. Mod. Phys.**45**, 178 (1973).

15. S. K. Allison, Rev. Mod. Phys. **30**, 1137 (1958).

16. H. Tawara, T. Kato, Y. Nakai, Atomic Data and Nuclear Data Tables (1985), 32(2), 235-303.

17. H. Betz. In "Atomic Physics: Accelerators", *Methods of Experimental Physics*, edited by P. Richard, Vol. 17 (Academic Press, New York, 1980), p. 73-148.

18. P.T. Greenland. Phys. Rep. **81**, 131 (1982).

19. G. D. Alton, L. B. Bridwell, M. Lucas, C. D. Moak, P. D. Miller, C. M. Jones, Q. C. Kessel, A. A. Antar, and M. D. Brown, Phys. Rev. A, **23** 1073 (1981).

20. S. A. Boman, E. M . Bernstein, and J. A. Tanis, Phys. Rev. A, **39**(9) 4423(1989).

21. R. Olson, Nucl. Instr. And Meth. A, **464** 93, 118 (2001).

22. D. Mueller, R. L. Watson, L. Grisham, I. Kaganovich, V. Horvat, K. E. Zaharakis, M. S. Armel, Physics of Plasmas. **8**(5) 1753 (2001).

23. L. H. Toburen, M. Y. Nakai, and R. A. Langley, Phys. Rev. **171**, 114(1968); H. Tarwara and A. Russek, Rev. Mod. Phys. **45**, 178(1973).

24. C. R. Kitchin, *AstrophysicalTechniques,* (Adam Hilger, Philadelphia, 1991).

25. H. Tawara and A. Russek, Rev. Mod. Phys. **45**, 178 (1973)**.**

26. S. Datz, H. O. Lutz, L. B. Bridwell, C. D. Moak, H. D. Betz and L. D. Elsworth, Phys. Rev. A **2**, 430 (1970).

27. G. I. Bell, Phys. Rev. **90**, 548 (1953).

28. R. E. Olson and A. Salop, Phys. Rev. A **14**, 579 (1976).

29. N. Bohr, Kgl. Danske Videnskab. Selskab, Mat.-Fys. Medd. **18**, No. 8. (1948).

30. N. Bohr and J. Lindhard, Kgl. Danske Videnskab. Selskab, Mat.-Fys. Medd. **28**, No. 7. (1954).

31. W. G. Graham, K. H. Berkner, R. V. Pyle, A. S. Schlachter, J. W. Stearns, and J. A. Tanis, Phys. Rev. A **30**, 722(1984).

32. R E Olson, R L Watson, V Horvat and K E Zaharakis, J. Phys. B: At. Mol. Opt. Phys. **35** 1893–1907 (2002).

33. R. E. Olson, Nucl. Instr. And Meth. A **464** 93-97 (2001).

34. D. S. F. Crothers and N. R. Todd, J. Phys. B **13**, 2277 (1980).

35. H. Knudsen, H. K. Haugen and P. Hvelplund, Phys. Rev. A **23**, 597 (1981).

36. A. S. Schlachter, J. W. Stearns, W. G. Graham, K. H. Berkner, R. V. Pyle, and J. A. Tanis, Phys. Rev. A **27**, 3372 (1983) .

37. W. G. Graham, K. H. Berkner, E. M. Bernstein, M Clark, R. H. McFarland, T. J. Morgan, A.S. Schlachter, J. W. Stearns, M. P. Stockli and J. A. Tanis, J. Phys. B **18**, 2503 (1985) .

38. S. H. Be, T. Tonuma, H. Kumagai, H. Shibata, M. Kase, T. Kambara, I. Kohno and H. Tawara, J. Phys. B **19**, 1771 (1986).

39. S. Datz, R. Hippler, L. H. Andersen, P. F. Dittner, H. Knudsen, H. F. Krause, P. D. Miller, P. L. Pepmiller, T. Rosseel, R. Schuch, N. Stolterfoht, Y. Yamazaki and C. R. Vane, Phys. Rev. A **41**, 3559 (1990).

40. O. Heber, G. Sampoll, B. B. Bandong, R. J. Maurer, R. L. Watson, I. Ben–Itzhak, J. M. Sanders, J. L. Shinpaugh, and P. Richard, Phys. Rev. A **52**, 4578 (1995).

41. J. H. McGuire and L. Wever, Phys. Rev. A **16**, 41 (1977).

42. V. A. Sidorvich, J. Phys. B **14**, 4805 (1981).

43. O. Heber, R. L. Watson, G. Sampoll, and B. B. Bandong, Phys. Rev. A **42**, 6466 (1990).

44. Heber, G. Sampoll, B. B. Bandong, R. J. Maurer, R. L. Watson, I. Ben–Itzhak, J. M. Sanders, J. L. Shinpaugh, and P. Richard, Phys. Rev. A **52**, 4578 (1995).

45. J. P. Desclaux, Computer Physics Communications **9** 31-45(1975).

46. Data for bondlength comes from the following website: http://web.mit.edu/3.091/www/pt/pert1.html, successfully accessed on March 21, 2003.

47. Data for the radius of atoms comes from the following website: http://www.webelements.com/webelements/elements/text/H/radii.html, successfully accessed on March 21, 2003.

VITA

Yong Peng was born in 1970 in Hanyuan, Sichuan, China. He received his B.S. diploma in chemistry from Sichuan University in 1994. Then he worked in CAEP, China. In 1997, he started his MS study at the University of Science and Technology of China. Supported by the Welch Foundation, he began his current program at Texas A&M University in 1999. His mailing address is 200 Charles Haltom Ave. 2H, College Station, TX 77840.